Metals and Materials International (2024) 30:2343–2371
https://doi.org/10.1007/s12540-024-01650-8

Selective Laser Melting of Stainless Steels: A review of Process, Microstructure and Properties

A. Mansoura[1] · N. Omidi[1] · N. Barka[1] · Sasan Sattarpanah Karganroudi[2] · S. Dehghan[1]

Received: 3 October 2023 / Accepted: 7 February 2024 / Published online: 23 March 2024

Abstract
Metal additive manufacturing is revolutionizing how we produce and use materials. Selective Laser Melting (SLM) is one of the most popular additive manufacturing techniques for creating high-performance metal components. Stainless Steel is preferred for additive manufacturing due to its powder form availability, low cost, mechanical properties, and corrosion resistance. However, the complex thermal history and rapid solidification in the SLM process led to an out-of-equilibrium microstructure of resulting components, which can affect their mechanical properties. To better understand the relationship between processing, microstructure, and properties, exploring and enhancing SLM-fabricated stainless-steel components is essential. This review comprehensively overviews the selective laser melting process, key processing parameters, and commonly encountered defects. Furthermore, the study presents a detailed discussion of microstructure, mechanical behavior (including hardness, tensile, and fatigue properties), and corrosion resistance of all SLM-manufactured stainless steel grades, along with the effects of various post-process treatments. This paper reveals that the SLM process can produce stainless steel with satisfactory performance that may exceed conventionally processed materials. However, the final section highlights the challenges and research gaps in this field that must be addressed.

Keywords METAL additive manufacturing · Selective laser melting · Stainless steel · Review · Microstructure · Mechanical properties

1 Introduction

Metal additive manufacturing is gaining interest, with three types of systems: powder-bed, powder-feed, and wire-feed. Selective laser melting (SLM) is a popular powder-bed fusion process that selectively melts metal powder using a laser beam as shown in Fig. 1 [1]. Their common feature is to build-up parts layer upon layer, based on 3D model data, achieving in that way a near-net shape, as opposed to traditional subtractive manufacturing methods [2]. This unique feature allows flexibility in design and geometry, elimination of expensive part-specific tooling costs, short lead-time, part-customization, functional integration, weight reduction, and cost-efficiency [3, 4]. These advantages, shown in Fig. 2, are particularly relevant to the replacement and customization of high-performance components for aerospace, medical, energy, and automotive applications [5]. Compared to conventional manufacturing processes, SLM offers great potential for improving material efficiency, reducing life-cycle impacts, and achieving sustainability [6].

SLM is versatile and can process various materials [7], including stainless steel, which is widely used due to its properties and low cost [8]. However, challenges related to physical phenomena and thermal cycling of the material powder remain. This review focuses on the SLM process and its application to stainless steel, examining microstructure, mechanical and fatigue properties, and corrosion resistance. The article also compares SLM and conventionally produced material properties and presents the effects of post-process treatments on SLM-processed stainless steels. The aim of this paper is to fill the gap by providing a complete insight into the microstructural evolution and its impact on the

✉ S. Dehghan
shayan.dehghan@uqar.ca

[1] Department of Mathematics, Computer Science and Engineering, University of Quebec at Rimouski, Rimouski, QC G5L 3A1, Canada

[2] Department of Mechanical Engineering, University of Quebec at Trois-Rivières, Trois-Rivières, QC G8Z 4M3, Canada

mechanical, fatigue, and corrosion performances of SLM stainless steels.

To allow the reader to gain a structured overview of SLM process and its application to stainless steels, this paper is organized as follows: Sect. 2 presents critical processing parameters, common process-induced defects, and environmental and economic impacts. Section 3 seeks to critically examine the microstructure, mechanical behavior (i.e. hardness, tensile strength, and fatigue properties), as well as corrosion properties, of each stainless-steel class (i.e., austenitic, martensitic/precipitation hardening, duplex, and ferritic) where enough data is available in the literature. Section 4 highlights the summary and provides an outlook on unexploited potential in the field of SLM processing of stainless steels.

2 Selective Laser Melting process

2.1 Process Parameters

In the SLM process, forming a fully dense product with well-overlapped continuous scan tracks involves many parameters and complex physical phenomena [9]. Some of the primary processing parameters are given in Fig. 3.

2.2 Defects in Selective Laser Melted Parts

Despite the unique capabilities of the SLM process, defects remain a critical issue that is frequently encountered in metal additive manufacturing components. These flaws adversely affect material properties and may lead to early failure as they act as stress concentrators under applied loads. This section briefly describes the formation mechanisms and mitigation strategies of some of the most challenging issues in SLM-fabricated stainless-steel components. Other defects, such as surface roughness, vaporisation of alloying elements, spatter and denudation, etc. exist; describing all of these in detail would lengthen this review excessively. The reader is referred to other reviews focused on defects [10–12]

2.2.1 Porosities and Lack-of-Fusion Defects

Pores can be categorized into gas pores from trapped gases, lack-of-fusion defects (LOF) from insufficient energy, and keyhole pores from excessive energy. Porosity can be minimized by selecting appropriate energy density and scanning strategy. HIP is commonly used as a post-treatment to close porosities and micro-cracks.

2.3 Balling

Balling is another typical defect affecting the quality of SLM parts. This happens when the laser beam used to scan the powder particles melts them into a cylinder of liquid metal, which can become unstable. The liquid pool can stretch out and break into tiny spherical beads, at high scanning speeds, to reduce surface energy [13, 14]. This is influenced by various factors, including the laser parameters used (such as scan speed, power, and layer thickness) and the properties of the powder material (such as melting point, density, and thermal conductivity) [15]. Relevant control methods reported in the literature include increasing input energy density (i.e., increasing laser power, lowering scan speed, and decreasing layer thickness), reducing the oxygen content in the atmosphere, adding a small amount of deoxidant, and employing laser re-melting techniques [16–18].

2.3.1 Residual Stress, Distortion and Cracking

Residual stresses arise from the large thermal fluctuations experienced by the solidified material due to the rapid heating and cooling cycles during the SLM process. These stresses are detrimental since they can lead to part distortion, cracking, and delamination of the fabricated metal part. As a result, the parts' dimensional accuracy and mechanical

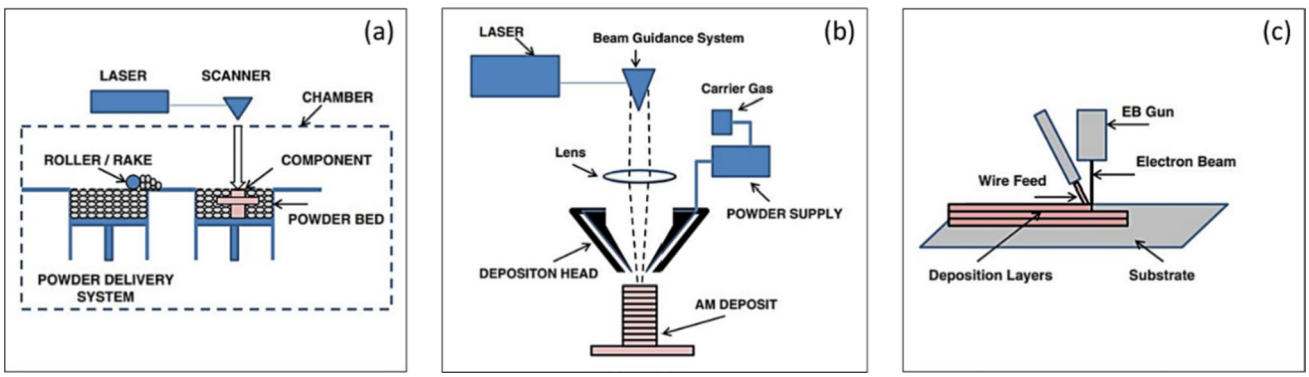

Fig. 1 Generic illustration of AM **a** powder bed system, **b** powder feed system, and **c** wire feed system. Reprinted with permission from Ref. [1]

Fig. 2 Advantages of SLM technology over conventional methods. Reprinted with permission from Ref. [165]

strength are affected [19]. These defects are a significant challenge in SLM because post-processing techniques cannot repair them. Thus, much research has been done to measure, model, predict, and mitigate residual stresses in SLM-produced stainless steel [18, 20–25]. A deep knowledge of the thermal stress evolution during the LPBF process is necessary to comprehend and alleviate the problems mentioned above. Mitigation strategies for residual stresses can be categorised into in-situ methods, such as substrate and/or feedstock powder preheating, laser rescanning, and post-processing methods such as stress relief heat treatment, shot peening and laser shock peening.

3 Environmental and Economic Aspects

The adoption of SLM holds considerable promise for both environmental sustainability and economic efficiency compared to conventional manufacturing processes (CM). In terms of environmental impact, SLM's additive approach significantly reduces material waste and allows for efficient weight reduction, a stark contrast to traditional subtractive methods such as milling and turning. Additionally, SLM can decrease the cradle-to-gate environmental footprints of parts by eliminating the need for tools, dies, and lubricants. Studies on the sustainability of SLMed components have already been conducted aiming to quantify and minimize the environmental impact [26]. Wang et al. [27] made a comparative life cycle assessment (LCA) of a SLM-produced hydraulic valve body. It was discovered that the SLM had a 37.42% lower environmental impact. The SLMed optimal design can further reduce environmental impacts by 16.84%. The

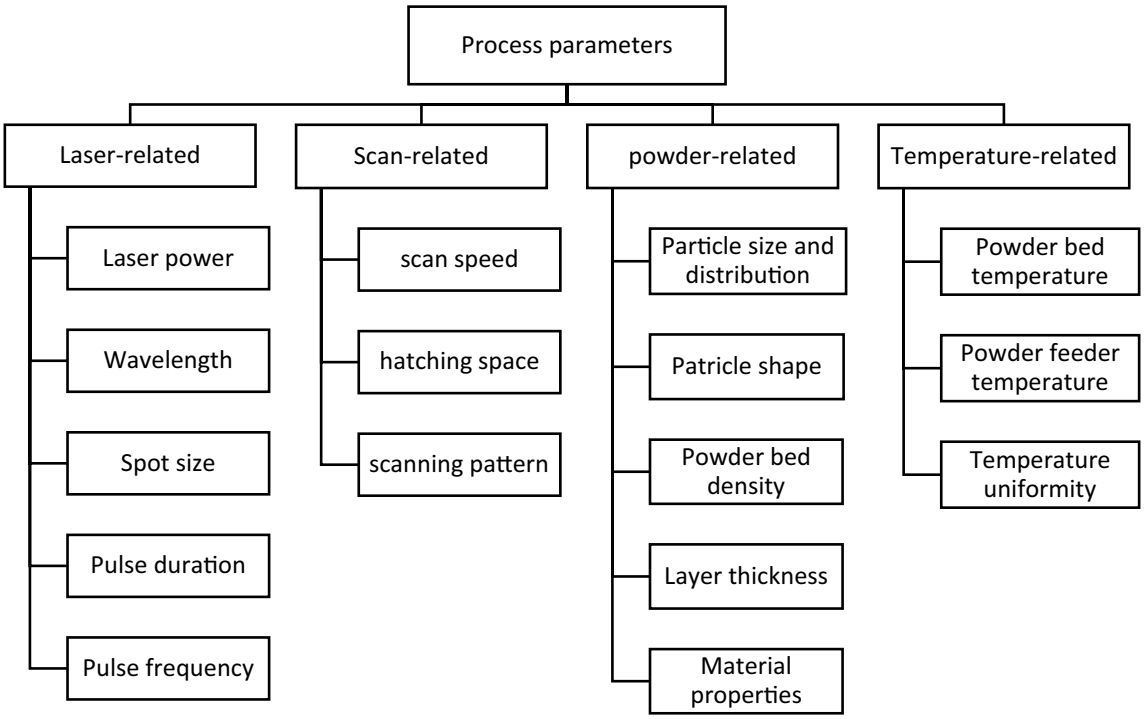

Fig. 3 The principal process parameters controlling part quality in the SLM process. Reprinted under Creative Commons CC-BY license from Ref. [166]

study also highlighted that powder preparation and energy consumption are the main reasons of SLM environmental impact. Huang et al. [28] estimated the energy and greenhouse gas emissions saving potentials for lightweight aircraft parts with the use of SLM and other AM technologies, as shown in Fig. 4. The cumulative CO_2 emissions reduction was estimated at 92.8–217.4 million tons. Economically, SLM offers a streamlined and cost-effective alternative. The elimination of complex tooling and setup costs, often associated with the production of intricate components in conventional manufacturing, is a noteworthy advantage. Rickenbacher et al. [29] developed a specific cost model for SLM, showing that building multiple parts at the same time instead of using separate builds may reduce costs by 41%. In another study, Huang et al. [30] found that adopting SLM over CM for injection molds can result in notable savings of 12%–60% in lead time, 70%–80% in downtime, and 15%–35% in overall costs over 1 million injection molding cycles. Therefore, the environmental benefits coupled with the economic advantages position SLM as a compelling and sustainable solution for stainless-steel manufacturing, especially for complex geometries and spare parts. However, more work is required.

4 Stainless Steels in Selective Laser Melting

Stainless steels are usually classified into subcategories: ferritic, austenitic, martensitic, duplex, and precipitation hardening [31]. Depending on the thermal history and the composition, microstructural and crystallographic features distinguish SS grades from each other's. During the last two decades, there has been a rapid increase in publications related to the SLM process of stainless steel. To date, different grades of stainless steel have been successfully implemented in L-PBF systems with superior mechanical properties compared to conventionally processed stainless steel. However, process control and standardization issues hinder the adoption of SLM technology. A deeper understanding of process-structure–property relationships and machine-to-machine variability is required to ensure quality, consistency, and reproducibility [1]. The present paper provides an overview of commonly printed grades of stainless-steel powder.

4.1 Austenitic Stainless Steels

Austenitic stainless steels are the most common and most prominent family of stainless steel. A face-centered cubic (FCC) crystal structure is achieved by adding austenite-stabilizing elements such as nickel, manganese, and nitrogen to maintain phase stability at all temperatures [32]. This steel class is highly attractive in the marine, chemical, petrochemical, food, and biomedical industries because of its good ductility, toughness, corrosion resistance, and its biocompatibility. The additive manufacturing of austenitic stainless steels is widely investigated in the literature. The published papers on austenitic stainless steels processed by SLM deal essentially with 316L stainless steel and less with 304L. The chemical compositions of these two common grades are given in Table 1. Adding 2% of molybdenum in 316L provides greater resistance to acids and localized corrosion

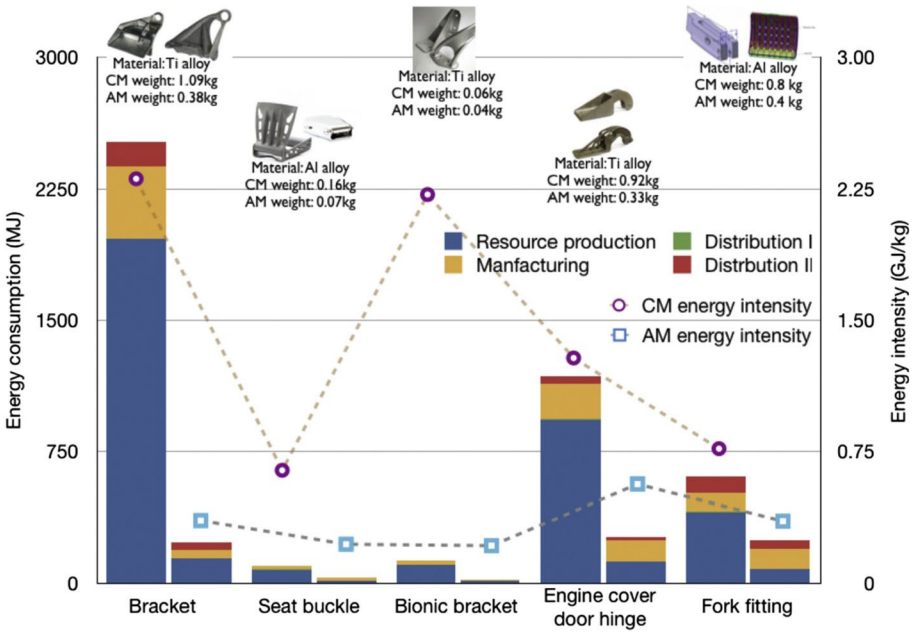

Fig. 4 Cradle-to-gate primary energy results for aircraft components. Reprinted with permission from Ref. [28]

such as pitting and crevice corrosion compared to 304L. The lower Ni and Mo content in 304L, which are expensive alloying elements, reduces prices. Therefore, 304L is commonly used instead of 316L if the service environment is less harsh.

4.1.1 Microstructure of SLM-Produced Austenitic Stainless Steels

Selective laser-melted parts are formed through rapid solidification rates, high thermal gradients, and repetitive heating and cooling cycles, resulting in a unique microstructure out of equilibrium [33]. The SLM parameters modulate the thermodynamic mechanisms that govern the formation and evolution of key microstructural features, including the solidification morphology, grain size, crystallographic texture, secondary phases, etc. [34]. Austenitic stainless steels produced by SLM usually show a pure FCC austenite phase [35–44]. Nevertheless, few works have reported a small fraction of the δ-ferrite phase [45–50]. The chemical compositions of the 316L and 304L stainless steel powders with a relatively high Cr_{eq}/Ni_{eq} ratio promote austenitic-ferritic (AF) or ferritic-austenitic (FA) solidification modes [51, 52]. In the case of AF mode, austenite precipitates as a primary phase with subsequent ferrite formation in the intercellular regions according to the sequence $L \rightarrow (L+\gamma) \rightarrow (L+\gamma+\delta) \rightarrow (\gamma+\delta)$ [45, 51]. In the case of the FA mode, solidification starts with the nucleation of δ-ferrite, followed by the formation of austenite in interdendritic regions. Through further cooling, δ-ferrite undergoes peritectic transformation to austenite. Due to the high cooling rate of SLM process, the peritectic reaction could not be completed and partial δ-ferrite is retained in the austenite matrix [48, 53]. The cooling rate strongly influences the ferrite's morphology and volume fraction, which can be controlled by process parameters such as laser power and scanning strategy [45, 51].

icrostructural characterization performed in the literature [43, 48, 50, 54–58] on 304L and 316L austenitic stainless steels reported a hierarchical microstructure with common features at multi-length scales as illustrated in Fig. 5. The difference between wrought and SLMed 316L microstructure is clearly visible in Fig. 6.

At the micron scale, columnar grains, ranging between 10 and 100 µm, are observed within the melt pools, growing epitaxially in the thermal gradient direction. High-angle grain boundaries delimit them. The layer-by-layer nature of the SLM process promotes epitaxial grain growth during solidification as the previously solidified grains provide a ready nucleation site for the melted material. Moreover, the heat transfer along the building direction is higher than thermal conductivity through the metal powder or heat convection with the building environment, leading to directional solidification. As a result, large columnar grains are usually formed along the build direction, normal to the solidifying surface of the melt pool [59, 60].

At the sub-micron scale, an intragranular cellular solidification structure delineated by segregation of heavy alloying elements, such as Mo and Cr, and high dislocation density at the cell walls is seen within the individual large grains. Cells have a size of 1 µm or less and an elongated or polygonal (equiaxed) shape depending on their growth direction. The formation mechanism of the intragranular cellular network is often explained in the literature by compositional fluctuations and constitutional supercooling [43, 54, 61]. According to solidification theory, the the temperature gradient G and the solidification rate R can control the microstructure. The ratio G/R determines the morphology of the solidification structure (planar, cellular, columnar dendritic, and equiaxed dendritic) while the product $G \times R$ (which defines the cooling rate) determines the size of the solidification structure [5]. At a relatively high numerator ratio G/R, the cellular dendritic structure is favored, which is the case of the SLM process. A higher cooling rate $G \times R$can achieve a finer microstructure. Several investigations [40, 62] found that a low energy density (i.e., low laser power and/or high scan speed) leads to a high cooling rate, resulting in a refined primary dendrite spacing. (See Figs. 7 and 8).

At the nanoscale, amorphous oxide inclusions are usually formed along the cell walls and in the matrix. These randomly dispersed nanoparticles, with a size up to several hundred nanometers, are mainly enriched in O, Si, and Mo, as shown in Fig. 9. Their formation is ascribed to the reaction between Si present in the precursor powder with the residual oxygen in the building chamber [41].

In SLM-produced austenitic stainless steels, a firm $<001>$ crystallographic fibre texture aligned along the building direction is typically observed [63, 64]. This direction is known to be the preferred crystallographic direction for cubic materials. Thus, columnar grains with an easy growth direction aligned to the maximum heat

Table 1 Nominal chemical composition of austenitic stainless-steel powder commonly used in SLM [167]

Grade name	Composition (wt%)								
	Fe	C	Cr	Ni	Mo	Mn	Si	P	S
AISI 316L	Bal	< 0.03	16.00–18.00	10.00–14.00	2.00–3.00	< 2.00	< 1.00	< 0.045	< 0.03
AISI 304L	Bal	< 0.03	18.00–20.00	8.00–12.00	–	< 2.00	< 1.00	< 0.045	< 0.03

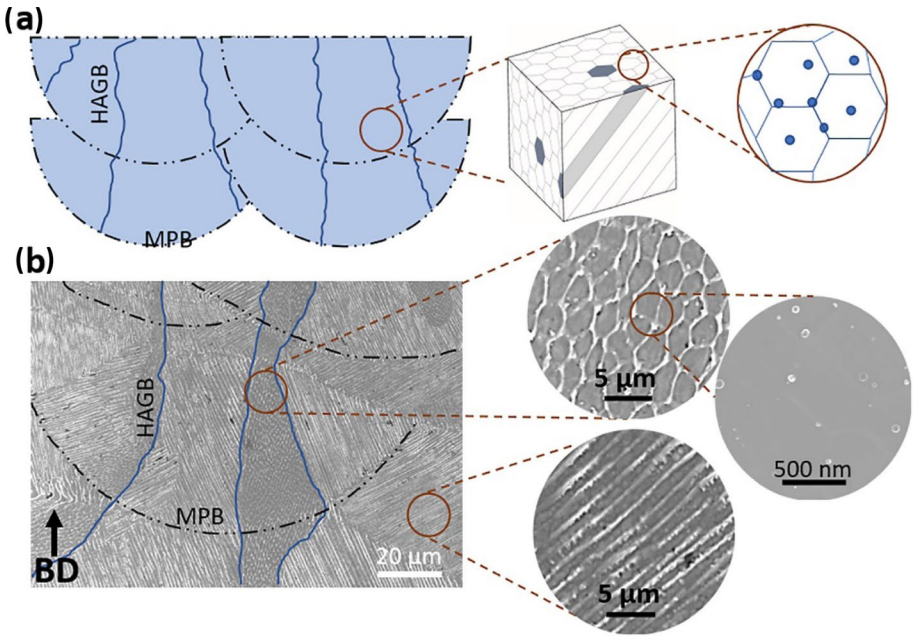

Fig. 5 Hierarchical microstructure of SLM-fabricated 316L stainless steel showing **a** schematic drawing of the melt pool boundaries (MPB), high angle grain boundaries (HAGBs), cell structure in 3D, and nano-sized oxide inclusions, **b** corresponding SEM micrographs of the microstructural features. Reprinted with permission from Ref. [58]

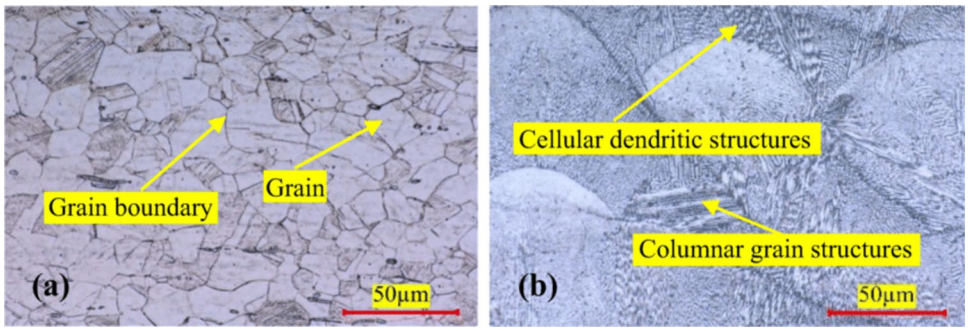

Fig. 6 The microstructure of **a** wrought 316L and **b** SLM-built 316L material from Ref. [72]

flow direction are formed due to competitive epitaxial growth [5, 48, 61]. However, microstructure formation with random texture has also been reported [36, 65]. It has been shown that texture depends on the local heat flow directions and the geometric features of the melt pool that are determined by processing parameters [66]. The influence of scanning strategy, laser energy density, and laser power on texture has been widely investigated [45, 47, 48, 67, 68]. Efforts are being made to achieve superior mechanical properties by controlling crystallographic texture [69, 70]. For example, Sun et al. [71] obtained a tailored $<011>$ crystallographic texture instead of the common $<001>$ crystallographic texture by using higher laser power and a bidirectional scanning strategy (see Fig. 10). Their approach enabled the activation of nano-twinning deformation mechanisms, resulting in enhanced strength and ductility.

Investigations into post-process heat treatment of SLM austenitic stainless steels revealed that as-built microstructural features remain stable up to 800 °C [61, 72–75]. At higher temperatures, the melt pool boundaries, cellular sub-structure, and dislocations disappear entirely, as seen in Fig. 11. Hot isostatic pressing (HIP) resulted in the complete recrystallization of grains [76]. Phase composition may also be altered due to post-treatment. Kurzynowski et al. [45] observed the precipitation of σ-phase after stress relieving at 800 °C for five hours activated by ferrite and residual stresses in as-built 316L. Saeidi et al. [73] reported the occurrence of phase transformation from almost pure austenite to a dual austenite/ferrite structure following annealing at 1100 °C.

4.1.2 Microhardness and Mechanical Properties of Austenitic Stainless Steels

This section reviews the strength, ductility, and microhardness of SLM-Built austenitic stainless-steel components emphasizing the process-structure-properties relationship. Due to the disparate devices, heat sources, and processing parameters used throughout the literature, volumetric

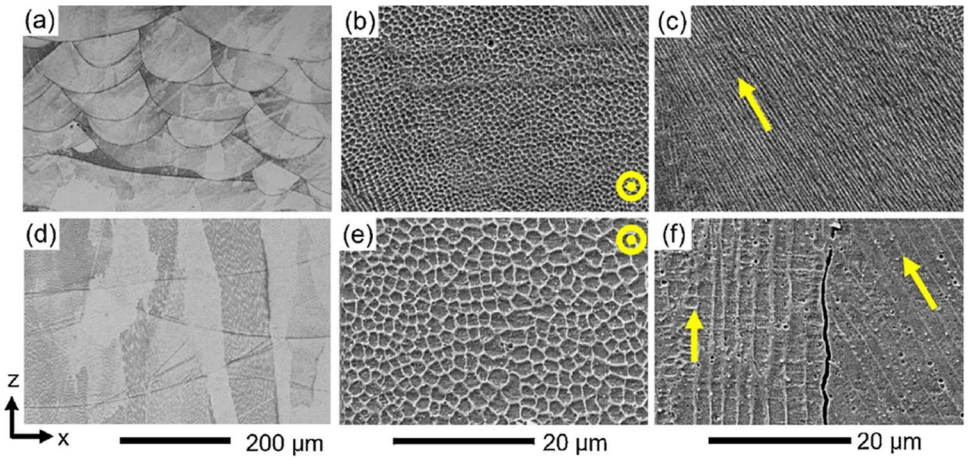

Fig. 7 Micrographs of 316L SS samples processed with low laser power (**a**, **b**, **c**) and high laser power (**d**, **e**, **f**). (**a**, **d**) show melt pools and columnar grains, (**b**, **e**) show cells growing parallel, and (**c**, **f**) perpendicular to the XZ plane. The yellow arrow indicate the cell's growing direction. Reprinted with permission from Ref. [67]

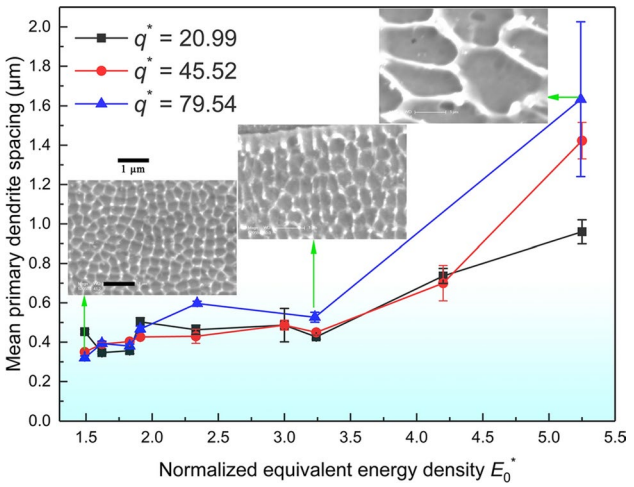

Fig. 8 Effect of laser energy density on primary dendrite spacing (cell size). Reprinted with permission from Ref. [62]

energy density is used to compare studies where possible. Table 2 lists the obtained yield strength (Ys), ultimate tensile strength (UTS), elongation at failure (El), and microhardness (H) for 316L and 304L austenitic stainless steels fabricated by SLM in their as-built condition, along with the minimum standard requirements according to ASTM A240.

It can be observed that there is a large variability in the attained properties values from different ranges of laser energy density. This variation may be due to the different scanning strategies and processing parameters leading to different thermal histories [5]. The disparity in results is also due to the diverse build geometries and the process's inherent defects [77]. It has been shown that porosity hurts the strength of the material. Defects at weak regions act as stress raisers and promote micro-cracks formation under loading, leading to a brittle failure mode [78]. The summary in Table 2 also reveals the effect of building orientation on mechanical properties. Anisotropy of the mechanical properties is usually explained by morphological texture and columnar structure growing along the building direction due to directional solidification [36]. The horizontal build generally has higher yield and ultimate tensile strengths and lower elongation at failure than the vertical build [36, 70, 79, 80].

Despite the high variability of the reported results, SLM-produced austenitic steels often have superior yield strength and tensile strength in the as-built state, compared to annealed conventional counterparts. The yield strength demonstrated by SLM-built 316L and 304L SS was 400–660 MPa, two to three times higher than that of conventional material. Ultimate tensile strength has shown a relatively minor increase, being in the range of 460–800 MPa (compared to 485–620 MPa for conventional [81]). Interestingly, this exceptional increase in strength is achieved without loss of ductility. Although some researchers obtained lower elongation to failure, most studies reported elongation to failure in the range of 32%–67%. Thus, it is reasonable to claim that SLM-fabricated austenitic stainless steels demonstrate high strength and good ductility.

Figure 12 shows a comparison of yield stress versus uniform elongation for various 316L SS including conventional annealed material (in yellow) and SLM-printed material (in red). The improved yield strength of SLM material at similar elongation values, when compared to annealed traditionally manufactured material, is clearly visible. The outstanding combination of strength and ductility obtained in SLMed SS exceeds even that of high-performance 316L SS strengthened by nanotwin bundles [43].

In a comprehensive study conducted by Liverani et al. [41], the mechanical properties of austenitic stainless steel annealed bars were compared to those manufactured using Selective Laser Melting (SLM). The research emphasized the critical role of processing parameters, including laser power, build direction, and hatch spacing. Their study demonstrated that building orientation influence the mechanical properties. Particularly, optimal parameter selection, along

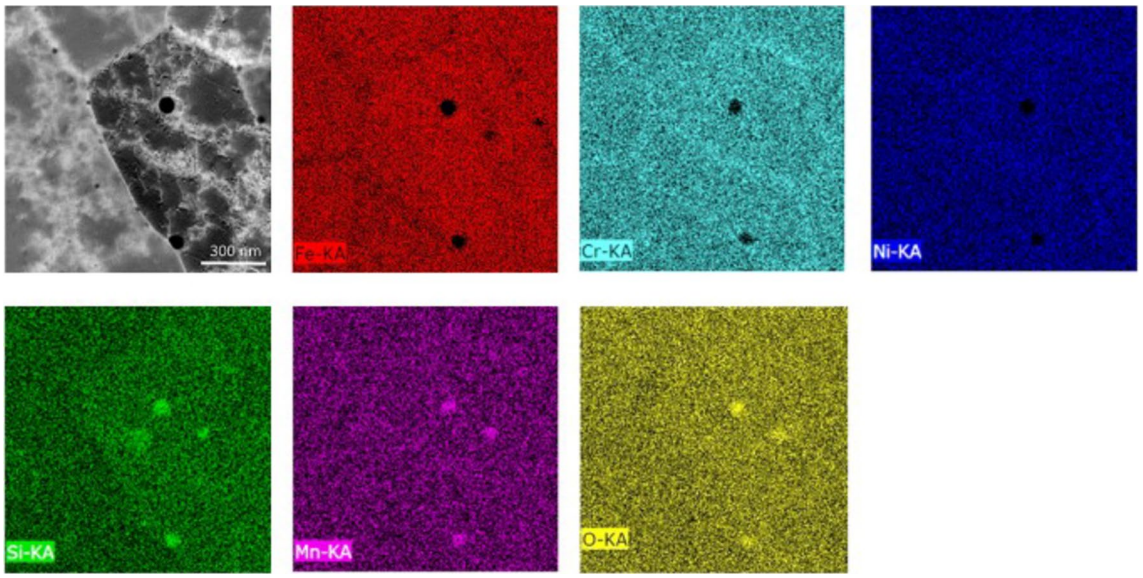

Fig. 9 HAADF STEM image with corresponding EDS elemental map showing micro-segregation of Cr at cell walls and Si-Mn–O rich nanoparticles in SLM 304L SS. Reprinted with permission from Ref. [48]

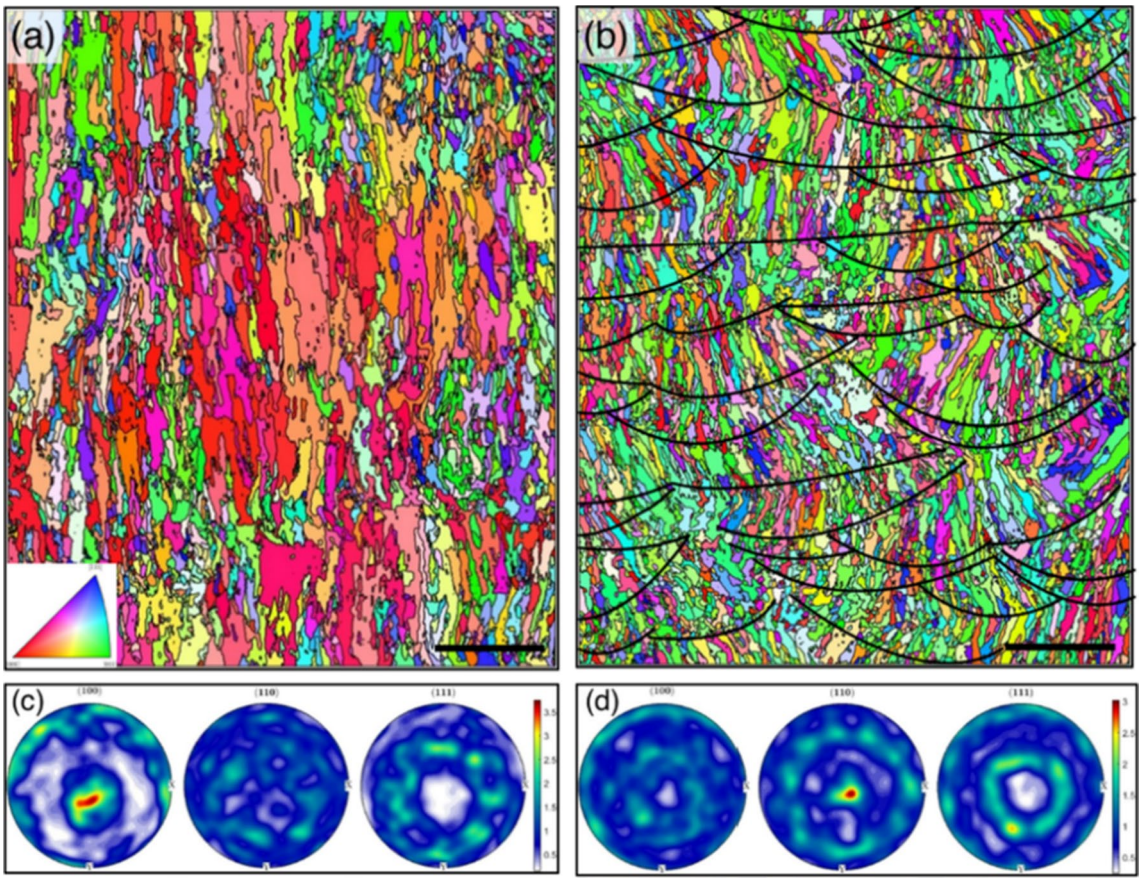

Fig. 10 EBSD IPF color maps with respect to build direction and their respective pole figures for the SLM-built 316L SS with laser power of (**a**, **c**) 380W and (**b**, **d**) 950W showing change of crystallographic texture from < 001 > to < 011 >. Adapted from Ref. [71] under Creative Common license (CC-BY 4.0)

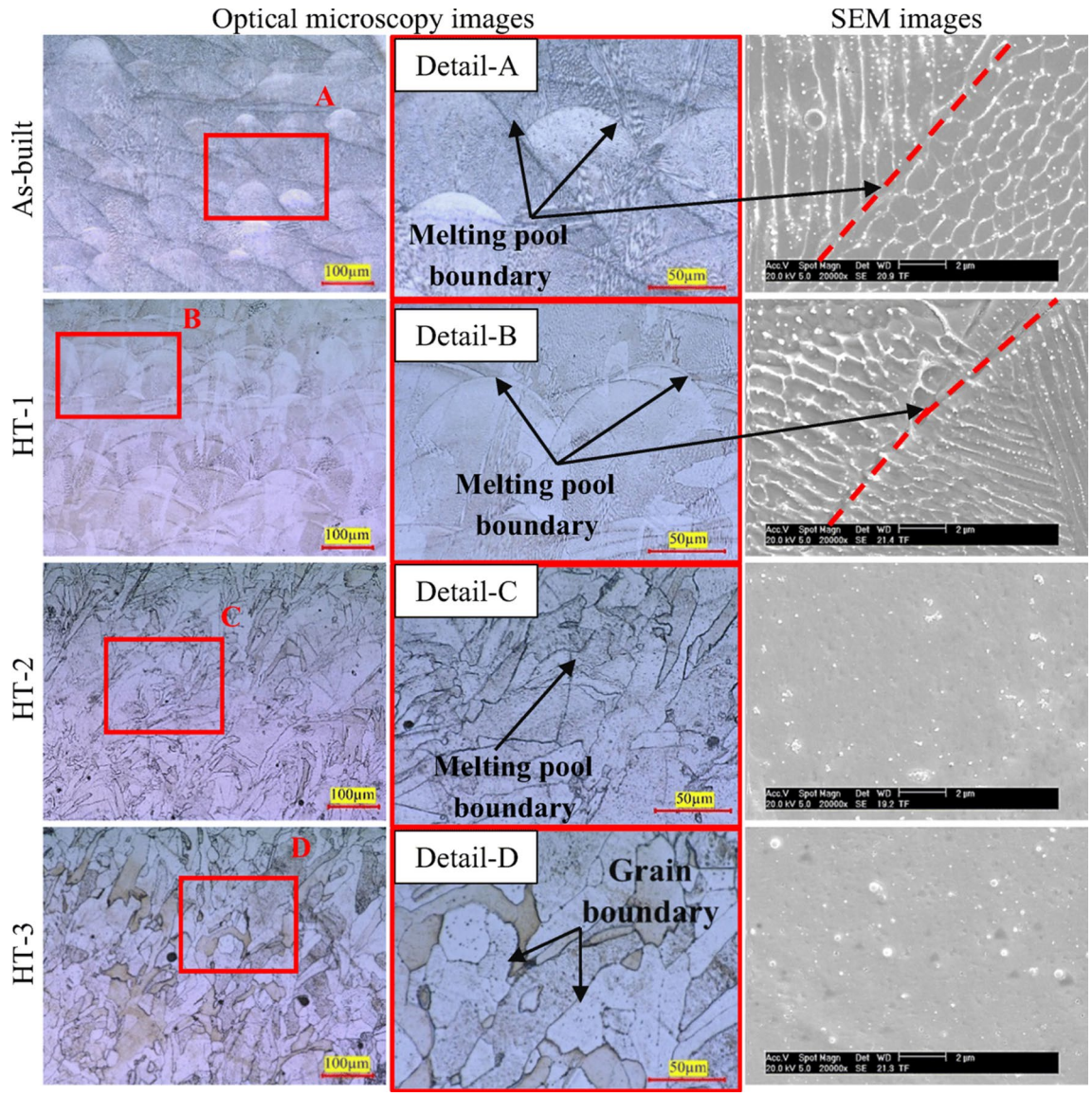

Fig. 11 The influence of heat treatment on the microstructure of SLM built 316L SS. (HT1 = 600° C/2h, HT2 = 850 °C/2h, and HT3 = 1100 °C/2h). Adapted with permission from Ref. [72]

with a 90-degree building direction, resulted in a remarkable improvement in elongation, reaching approximately 70% compared to machined and annealed bars with only around 50%. UTS of this SLM sample was comparable to that of conventional one (590 MPa vs 610MPa). The study further demonstrated the potential to enhance UTS up to approximately 640 MPa with an acceptable elongation of 40% by maintaining the same parameters but adjusting the building direction to 45 degrees.

This superior tensile strength in SLM-produced austenitic stainless steels is believed to originate from the unique hierarchical microstructure described in the previous section. All microstructural features will interfere with the dislocation movement [58]. The smaller grain size of the cellular structure leads to Hall–Petch strengthening since cell boundaries hinder the dislocation slips during deformation [43, 49, 56, 60]. Also, the high population of piled-up dislocations induced by rapid heating and cooling during the SLM process contributes significantly to material strengthening by hindering plastic deformation [39, 49, 70]. Moreover, the silicon-rich nano-inclusions may act as pinning points and halt the dislocation's movement, which results in a hardened austenitic steel [49, 54, 58].

In addition to the enhanced strength compared with that of their conventional counterparts, the SLM-built austenitic stainless steels exhibit comparable ductility due to a low but steady strain hardening rate at high-stress levels, which arises from the activation of multiple deformation

Table 2 Mechanical properties of austenitic stainless-steel grades fabricated by SLM

SS grade	Equipment	P [W]	V [mm/s]	E [J/mm^3]	Building direction	ρ [%]	Ys [MPa]	UTS [MPa]	El [%]	H [HV]	Refs
304L	Concept Laser M3linear	95	70	377	H	92.8	182	393	25.9	192	[35]
			90	293		91.6	156	389	22.1	196	
304L	Self-developed machine	200	25	–	H	100	540	704	38	–	[80]
					I		380	550	30		
					V		450	570	58		
304L	3D Systems ProX 300	182	1000	110.3	H	–	455	707	45	–	[50]
					V		410	665	55		
304L	Self-developed machine	200	800	125	H	99.98	500	800	48	250	[36]
					V		460	750	50		
304L	3D Systems ProX 300	200	1400	65	–	99.99	485	712	61	–	[168]
304L	ORLAS Creator	105	100	700	–	99	540	660	36	233–254	[48]
			400	175		97.5	430	530	32		
304L	EOS M290	220	1100	62.5	H	99.9	457	653	67	–	[49]
					V		411	612	72		
316L	Renishaw AM250	200	1000	40	V	≥ 99.8	487	594	49	228	[43]
316L	SLM 280HL	400	–	–	H	99.7	500	640	47	241	[67]
		1000				99.8	400	460	4.2	213	
316L	Dimetal-100	300	700–1200	104–178.6	–	≥ 98	–	530–590	15–21.1	260–281.6	[40]
316L	SLM 250 Realize MCP	200	Up to 1000	–	H	≥ 99.9	663	685	25	235	[79]
					I		649.3	669.3	35.6		
					V		557	591	42		
316L	Sisma MYSINT100	100–150	700	102–214.3	I	≥ 98	510–530	610–650	27–41	230	[41]
							425–490	550–580			
					V				42–71		
316L	M1 cusing	180	1600	53.57	H	96	397	668	37	226	[169]
	Concept Laser				V		387	564	35	221	
316L	SLM 280HL	200	800	69.4	H	≥ 99	516.5	634.4	33.2	226.7	[170]
					I		589.9	699	32.6	227.8	
					V		438.6	512	11.8	223.6	
316L	Renishaw AM250	200	5000	7.27	–	–	518–561	662–688	45.3–52.7	–	[39]
316L	Concept Laser	90	1000	20	H	97.7–98.1	512–536	622–668	20.4–24.7	–	[87]
					V		430–448	509–528	12.4–11.6		
316L	EP-M250	206	900	84.77	H	98.93	584	773	46	–	[62]
		360	2465	54.09		98.6	549	708	28		
316L	SLM 125HL	200	800	69.4	–	99.97	563	710	48.3	–	[42]
316L	EOS M290	195	800–1400	58–203.1	V	98.7–99.9	452–510	530–570	33–52	–	[58]

Table 2 (continued)

SS grade	Equipment	P [W]	V [mm/s]	E [J/mm^3]	Building direction	ρ [%]	Ys [MPa]	UTS [MPa]	El [%]	H [HV]	Refs
316L	4 different devices	73.5–148.8	300–1000	114.4–245	H	–	493	626	43	–	[55]
					V		446	551	46		

Standard reference values

Grade	Condition	YS [MPa]	UTS [MPa]	El. [%]	H [HRC]	References
316L 304L	Annealed-hot finished	175	485	40	155	[171]

H Horizontal (i.e. loading axis is perpendicular to build direction), *V* Vertical (i.e. loading axis is parallel to Build direction), *I* Loading axis is inclined by 45° with respect to the build direction

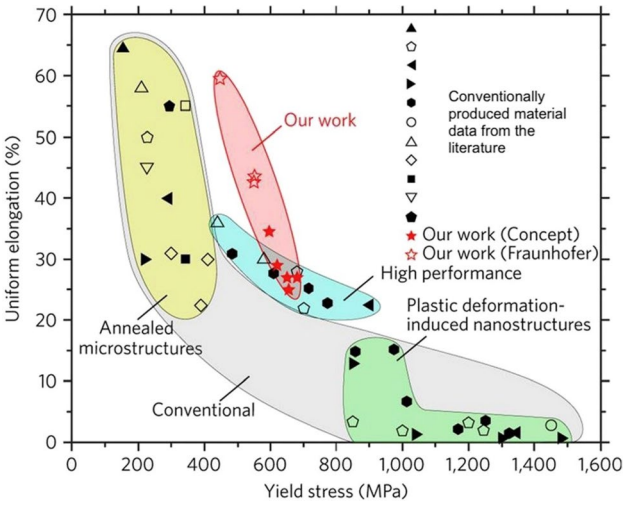

Fig. 12 Tensile properties of SLM produced 316L SS (in red) compared with conventionally produced material. Adapted with permission from Ref. [56]. (Color figure online)

mechanisms, such as dislocation slips, cellular wall evolution, and deformation twining [50, 70]. Many researchers [39, 48, 50, 56, 60, 70, 71] have demonstrated that SLM-processed austenitic stainless steels have evaded the strength-ductility trade-off thanks to twinning-induced plasticity. The interaction of the twin boundary and dislocation increases the dislocation storage capacity, simultaneously enhancing strength and ductility [48]. Besides the TWIP effect, a strain hardening by transformation-induced plasticity (TRIP) was also reported in 304L exclusively due to its low Ni content, an austenite stabilizer [50, 82].

According to the available literature, the average Vickers hardness values for SLM fabricated 304L and 316L stainless steels range from 200–280 HV, significantly higher than that of annealed counterparts (≈ 155HV). Similarly to strength, the superior hardness is attributed to the unique microstructural features inherent to the SLM process. Tucho et al. [57] and Cherry et al. [83] investigated the correlation between laser energy density, porosity, and hardness. Both concluded that hardness is highly influenced by porosity level, which is controlled by laser energy density. When the energy density is optimum, fully dense material is produced, resulting in high hardness. Outside of the optimum range, defects like balling or lack-of-fusion are likely to form, which lowers hardness.

Several researchers have studied the impact of post-process treatments on the mechanical properties of SLM-built 316L ASS [72, 73, 76, 84, 85]. It has been shown that strength and hardness decrease with increasing annealing temperature due to grain coarsening. HIP significantly reduced yield strength but improved ductility [76].

4.1.3 Fatigue Properties of Austenitic Stainless Steels

The fatigue strength of SLM-processed austenitic stainless steels is a decisive factor for many applications, such as biomedical implants and aerospace components, which are subjected to cyclic loading. From the literature, it is already known that process-induced defects, along with surface roughness and residual stresses, can significantly degrade the high cycle fatigue performance of additively manufactured parts by causing stress concentration and early crack initiation [81, 86]. Generally, 316L and 304L ASS manufactured by SLM exhibit good fatigue performance, which is comparable to that of their conventionally produced counterparts [41, 63, 87–92]. Spierings et al. [89] investigated the influence of surface quality on the fatigue life of 316L. They found that the fatigue limit at R = 0,1 (stress ratio) increased from 200 to 269 MPa when surface roughness decreased from 10 µm to 0.1 µm by machining and polishing. Riemer et al. [63] studied the high cycle fatigue (HCF) performance and fatigue crack (FCG) of SLM-processed 316L SS in different testing conditions. The fatigue limit of the as-built specimen with a turned surface is comparable to that of conventional material. Stress relieving at 650 °C did not significantly influence on the fatigue strength because the microstructure remained stable at this temperature. Both as-built and stress-relived conditions showed anisotropic behavior for crack growth rate. When the crack growth direction is parallel to the building direction, the crack can quickly grow along the elongated grain boundaries, leading to a high FCG rate (Fig. 13b). For crack growth normal to the building direction, the crack path is more tortuous, which slowed the growth rate (Fig. 13a). On the other hand, HIP at 1150° C induced a drastic change in microstructure with partial recrystallization of grains. Thus, more isotropic crack propagation and a higher fatigue limit are observed (Fig. 13c). Zhang et al. [90] investigated the correlation between HCF properties and porosity. Their work showed that for 316L SS, porosity does not impinge on the HCF properties when processing is done within the optimum range (energy density in the range of 70–130 J/mm^3). This defect-tolerant behavior is believed to result from he high ductility of 316L SS.

4.1.4 Corrosion Resistance

Austenitic stainless steels are widely employed in applications requiring resistance to pitting and crevice corrosion, such as marine engineering and medical implants [93]. The corrosion properties of stainless steels depend on their microstructure and chemical composition [34]. Pitting corrosion events initiate near second-phase precipitates and alloy impurities such as manganese sulfide (MnS) inclusions [94]. MnS is a common impurity dispersed in the matrix of traditional austenitic SS that promotes stable pit initiation and growth [95]. Regarding additively manufactured material, Sander et al. [96] found that SLM-printed 316L is more resistant to stable pit initiation than wrought material, with a higher pitting potential and a lower metastable pit frequency. It is hypothesized that rapid solidification of the SLM process reduces the number and size of MnS inclusions. Accordingly, pitting susceptibility was lowered. This hypothesis was also confirmed by Chao et al. [94], who claimed that oxides/oxynitrides particles formed during the SLM process have a homogenous Cr composition and no MnS inclusions are present. However, the process's inherent porosity resulted in inferior repassivation. This is in agreement with other studies [97, 98]. Schaller et al. pointed out a significant enhancement in the pitting potential of polished SLM 304L, far exceeding that of polished wrought 304L. Kong et al. [99] reported that SLM 316L, formed at high laser power,showed a thicker passive film, higher pitting potential, and lower corrosion rate than the quenched 316L in simulated body fluid, which makes it a good candidate for biomedical implants. Laleh et al. [100]

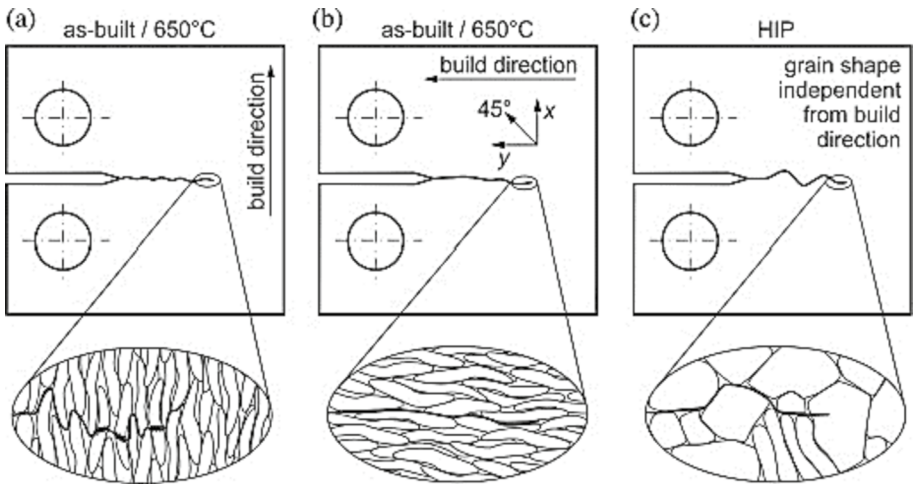

Fig. 13 Schematic illustration depicting the effect of grain orientation and morphology on crack propagation. Reprinted with permission from Ref. [63]

investigated the intergranular corrosion (ICG) resistance of SLM-produced 316L SS. The results reported in their work show a substantially higher IGC resistance of SLM 316L compared to its commercial counterpart. This behavior was related to the absence of localized Cr-depletion and the high number of fine grains with twin boundaries and low-angle grain boundaries.

The above-mentioned promising properties prove the efficiency of the SLM process in producing austenitic stainless steels with enhanced mechanical, fatigue, and corrosion properties, making them suitable for critical applications.

4.2 Martensitic and Precipitation-Hardening Stainless Steels

The martensitic family of stainless steels was developed mainly to satisfy the property requirements for high hardness, high strength, good wear resistance, and primary corrosion resistance [101]. They have an austenitic structure at high temperatures, but when quenched during heat treatment, a diffusion-less transformation occurs spontaneously to form a martensite structure [32]. Unlike ferritic and austenitic stainless steels, they are very amenable to heat treatment as they can be hardened by quenching and tempering to improve ductility and toughness [31]. These properties make them suitable for various of applications like medical tools, valves, pumps, bearings, cutlery, razor blades, injection moulds, etc. [102]. However, due to their relatively lower chromium content (generally between 11 and 18%), martensitic stainless steels are the most marginal corrosion resistant of all the stainless-steel alloys; their field of application is limited to only slightly aggressive environments [32].

The precipitation-hardening (PH) stainless steels are chromium-nickel grades that provide an optimum combination of the properties of martensitic and austenitic grades. The advantage of the PH alloys over the strictly martensitic stainless steels is that they attain great strength with higher toughness and corrosion resistance [32]. These improved properties are attributed to their higher chromium, nickel, molybdenum contents, and their restricted carbon level. PH stainless steels can be austenitic, semi-austenitic, or martensitic. However, martensitic PH steels are the most common in traditional and additive manufacturing. They are strengthened by the precipitation of a coherent second phase during aging heat treatment. Copper (Cu) and niobium (Ni) are the main hardening elements in martensitic PH stainless steels [103].

Among these alloys, 17–4 PH and 15–5 PH are the most commonly used martensitic PH stainless steels in metal additive manufacturing due to their good weldability and cost-effectiveness [104]. These specific alloys are widely employed in the aerospace, marine, nuclear, chemical, and petrochemical fields [105]. Recently, a few studies have been conducted on manufacturing 420 martensitic stainless by the SLM process as a promising material in tooling applications such as injection molds [106, 107]. The chemical composition of the reviewed alloys is given in Table 3. C-X stainless steel is another precipitation-hardening stainless steel, recently developed and commercialized by EOS Gmbh [108]. However, due to the lack of literature dealing with it, CX steel will not be further discussed.

In this section, the microstructure and performance of martensitic stainless steels processed by SLM will be discussed with a focus on precipitation hardening grades, particularly 17–4 PH and 15–5 PH SS, as they are the most researched in the literature. SLM of 420 martensitic steel will also be briefly discussed.

4.2.1 Microstructure of SLM-Fabricated PH Stainless Steels

The microstructure of SLM-fabricated PH stainless steels consists of overlapping melt pools with epitaxial columnar grains and an inner fine cellular-dendritic structure oriented parallel to the direction of heat flow and towards the center of the melt pool [109–111]. In addition to the large columnar grains, fine equiaxed grains tend to form at the melt pool boundaries, as shown in Fig. 14a, b [112–114]. This microstructural refinement is supposed to be the effect of several thermal cycles and rapid cooling on the recrystallization and/or local transformation of grains in the heat-affected zone [112, 114]. Generally, no Cu-precipitates are observed in the as-built microstructure of PH stainless steels, whereas Mn-Si-rich oxide inclusions have been widely reported [105, 115]. Several investigations into the as-built microstructure of PH stainless steels revealed a strong fibre $<001>$ crystallographic texture along the building direction (see Fig. 14a) [112, 116, 117]. However, texture-free material is also reported, mainly when bidirectional or rotating scanning strategies are used [113, 115, 118].

Unlike wrought PH stainless steels, which are fully martensitic, the SLM-fabricated PH stainless steels are said to comprise martensite, retained austenite, and even δ-ferrite. The reviewed literature shows a significant divergence among the results regarding phase composition and phase fractions of SLM-processed PH stainless steels. For instance, Facchini et al. [119] produced a mostly austenitic microstructure (72% austenite and 28% martensite) by selective laser melting of 17–4 PH stainless steel. Oppositely, Yadollahi et al. [120] and Nong et al. [121] reported a dominantly BCC martensitic structure with less than 7% of retained austenite in 17–4 PH and 15–5 PH SS, respectively.

Due to PH alloys' very low carbon concentration ($<0.07\%$), the martensite exhibits a nearly BCC structure like ferrite. Thus, the two phases cannot be distinguished by X-ray diffraction (XRD) and Electron Backscatter Diffraction (EBSD) [103]. Some recent studies [112, 117,

Table 3 Chemical composition of martensitic stainless-steel powders commonly used in SLM [167]

Grade name	Chemical composition (%w)									
	Fe	Cr	Mn	Ni	C	Si	P	S	Cu	Nb
17–4 PH	Bal	15–17.5	≤1.0	3.0–5.0	≤0.07	≤1.0	≤0.04	≤0.03	3.0–5.0	0.15–0.45
15–5 PH	Bal	14–15.5	≤1.0	3.5–5.5	≤0.07	≤1.0	≤0.04	≤0.03	2.5–4.5	0.15–0.45
AISI 420	Bal	12–14	<1.0	–	0.15–0.40	<1.0	<0.04	<0.03	–	–

122] claimed that the predominant BCC phase of columnar grains in the as-built 17–4 PH stainless steel is ferrite rather than martensite because no characteristics of martensitic microstructure, such as martensite laths or large misorientations, are observed in these grains. In these studies, small martensite blocks are found to be formed at the melt pool boundaries in the fine-grained zone along with FCC equiaxed austenite grains [112, 114].

Several explanations for the high variability in the reported results have been proposed. Recent studies have revealed that the chemical composition of the precursor powder plays a crucial role in the solidification mode and the resulting microstructure. Given their high Cr_{eq}/Ni_{eq} ratio, martensitic PH stainless steels typically solidify as primary δ-ferrite from the liquid state. During solidification, the δ-ferrite phase transforms to austenite upon cooling below

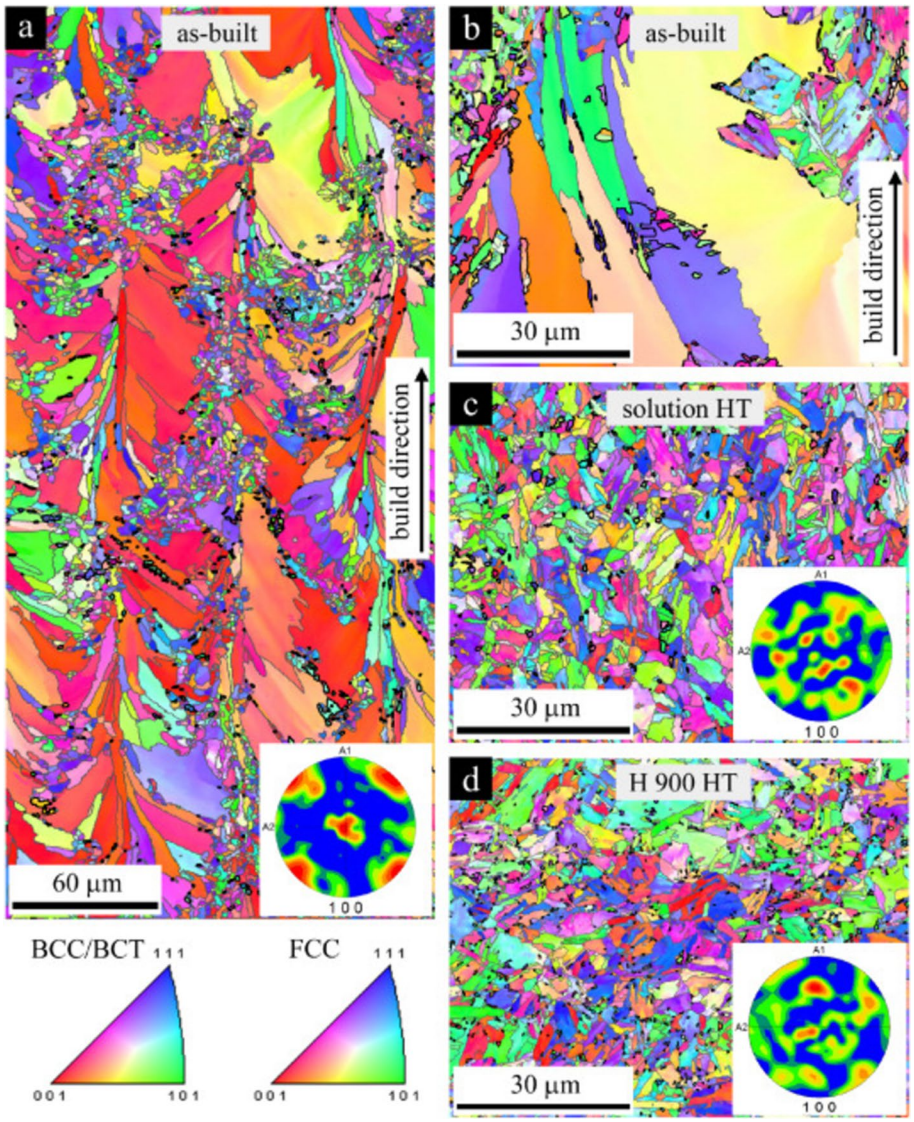

Fig. 14 EBSD orientation maps obtained from SLM processed 17–4 PH SS in different conditions: **a**, **b** as-built sample, **c** solution heat-treated sample, **d** H900 heat-treated sample. FCC/BCC phase boundaries are highlighted with bold black lines. Reprinted with with permission from Ref. [112]

the solidus temperature due to solid-state diffusion. Subsequently, when the martensitic start temperature (Ms) is reached, austenite to martensite transformation occurs until room temperature [117]. However, due to the high cooling rates in the SLM process, the $\delta \rightarrow \gamma$ transformation cannot be completed or might even be bypassed, therefore, the ferrite phase remains dominant at room temperature [117]. Vunnam et al. [116] demonstrated that ferrite-to-austenite transformation kinetics depend on the initial powder chemical composition, resulting in the microstructure and phase composition variability in the as-built condition. It has been shown that the residual δ-ferrite volume fraction decreases with decreasing the ratio Cr_{eq}/Ni_{eq} of the feedstock powder of PH stainless steels [116, 122]. On the other hand, the fraction of retained austenite compared to martensite has been of particular interest in the SLM of PH stainless steels as it strongly affects the mechanical properties. The retention of this metastable phase is commonly attributed to the large strain at grain boundaries, the high dislocation density, the fine grain size and interdendritic spacing, the concentrations of the alloying elements, and the supersaturation of the austenitic phase with stabilizing elements [109, 111]. Any of these factors would lower the Ms temperature to room temperature or below, which leads to the incomplete transformation of austenite to martensite [110]. In this context, several studies investigated the effects of atomizing medium and building chamber atmosphere on the final microstructure of PH stainless steels processed by SLM [111, 123, 124]. It has been shown that using nitrogen gas for powder atomization and/or as a shielding gas in the build chamber results in higher fractions of retained austenite. The formation of retained austenite appears likely due to the entrapment of nitrogen, which has an austenite stabilizing effect [111]. Microsegregation resulting from rapid cooling could also induce a localized concentration of austenite stabilizing elements such as Ni in the intercellular areas [103]. Variability in the retained austenite fractions in SLM-processed PH stainless steels has also been related to other processing parameters such as scanning strategy [121, 125], and building direction [113, 120]. These studies revealed that thermal history affected the retained austenite concentration in SLM fabricated parts. Nong et al. [121] studied the effect of different scanning strategies on the microstructure of SLM-fabricated 15–5 PH stainless steel. They found that complex thermal cycling and finer grain size in the island scanned led to more significant amounts of retained austenite. In a recent study, Lv et al. [105] found that the austenite volume fraction in SLM 15–5 PH decreased with built height. These findings were explained by the fact that the bottom specimen (i.e., bottom layers) experienced an in-situ heat treatment due to thermal cycling promoted by the fusion of subsequent layers of material, which resulted in the reversion of martensite to austenite.

Several studies focused on the effect of heat treatment on SLM-processed PH stainless steels. Different standard and non-standard heat treatments were investigated. For wrought 17–4 PH and 15–5 PH, a solution heat treatment is typically applied in the austenitic domain (~1050 °C), followed by quenching, to obtain a fully martensitic structure. This solutionized condition is often called 'condition A' (CA). A subsequent aging treatment in the range 480–620 °C is conducted, which results in precipitation hardening by copper precipitates. Precipitation begins with small and coherent spherical Cu-clusters with a BCC structure, which transform into an elliptical incoherent FCC structure, called ε-Cu upon overaging [126]. Many studies reported that solution heat treatment relieved the residual stress and homogenized the microstructure of SLM-fabricated PH stainless steels [112, 118, 127]. Sun et al. [112] found that solution heat treatment removed the <001> texture of the as-built microstructure and reduced the volume fraction of retained austenite, leading to a more conventional fully martensitic structure (Fig. 14). Their comparison between SLM and wrought material in condition A showed a similar microstructure with a finer grain size in the SLM heat-treated sample, which was attributed to the higher volume fraction of oxide inclusions and carbides that pinned grain boundaries. Nong et al. [127] reported that SLM and wrought 15-5PH demonstrated a similar precipitation behavior for copper in size and volume density upon H900 standard heat treatment, as shown in Fig. 15. The amount of retained austenite increased slightly during aging heat treatment due to the reversion of martensite. However, direct aging without prior solutionizing induced a higher fraction of reverted austenite due to the segregated austenite stabilizing elements in the as-built microstructure [115, 122]. Figure 16 summarizes the microstructural evolution of SLM-printed 17–4 PH stainless steel under different conditions. As can be observed, the as-built microstructure contained a matrix of fine packet of martensite and retained austenite with nano-oxide dispersion. Standard H900 heat treatment with prior solutionizing increases the fraction of martensite and induces ultrafine reverted austenite and Cu-rich precipitation phase. Direct aging increases fractions of reverted austenite and induces some Cu-rich precipitations.

4.2.2 Mechanical properties of as-built and heat-treated PH stainless steels

The hardness and tensile properties of 15–5 PH and 17–4 PH martensitic stainless steels processed by SLM are summarized in Table 4. A large dispersion of the mechanical property values is observed due to the high variability in phase composition and phase fractions discussed

previously. SLM-built PH stainless steels show lower strength and hardness than their peak-aged counterparts and superior elongation at failure. This behavior is related to the retained austenite and the absence of Cu-precipitates. LeBrun et al. [128] investigated the effect of retained austenite on the mechanical properties of SLMed 17–4 PH stainless steel. They found that tensile strength and hardness decrease with increased volume fraction of the retained austenite. At the same time ductility is enhanced due to the stress-induced transformation of metastable austenite to martensite [128]. Appropriate heat treatment is needed to improve the strength of SLM-processed PH stainless steels by reducing the retained austenite and promoting the precipitation of copper [120]. Following standard solutionizing and subsequent aging heat treatment at 480 °C for one hour (referred to as H900), SLM-processed PH SSs exhibited higher yield strength, higher ultimate tensile strength, and higher hardness than those of aged conventional materials [115, 127, 128], due to the strengthening effect of coherent Cu precipitates and nano-oxide

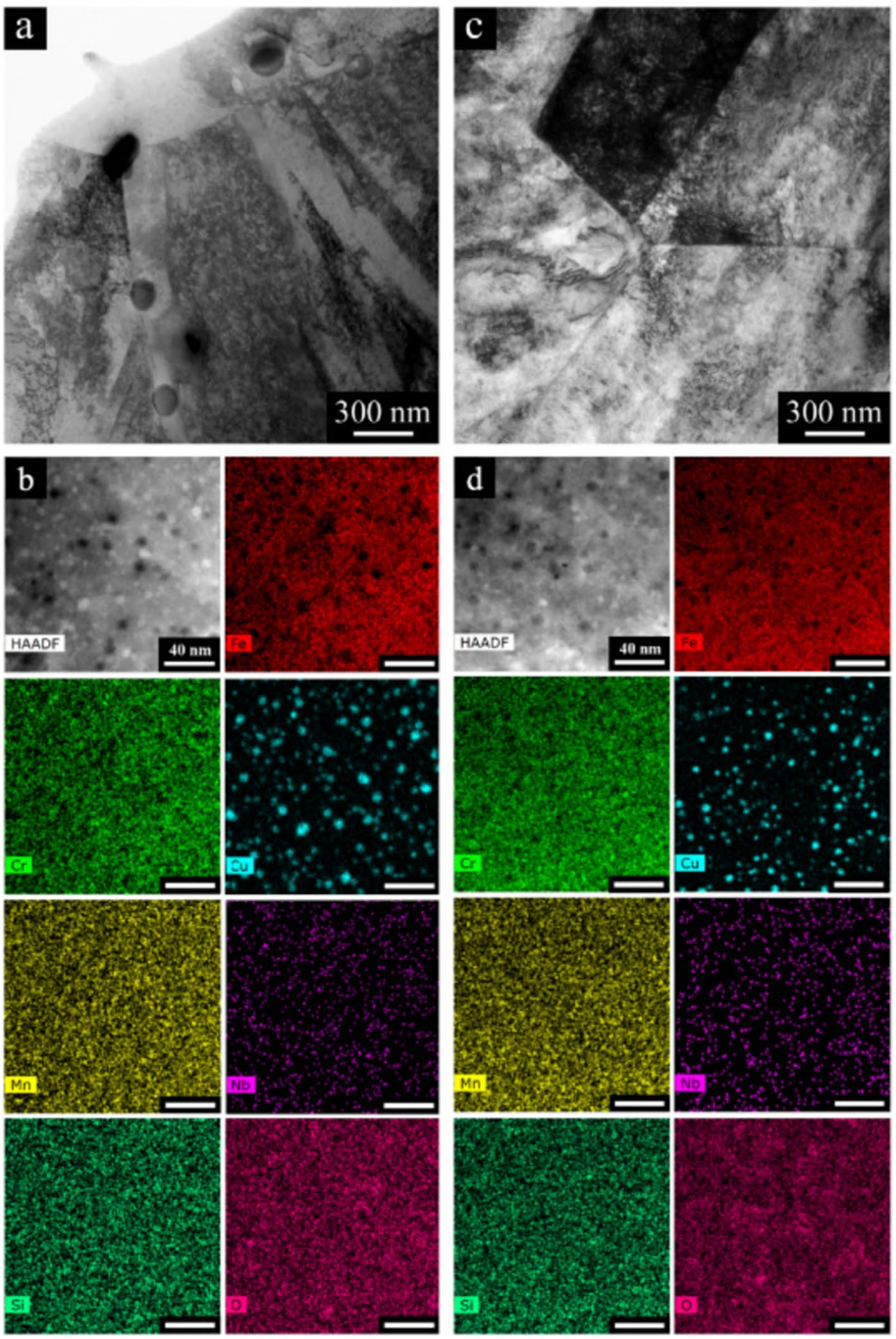

Fig. 15 STEM data of the H900 aged SLM sample (**a**, **b**) and wrought sample (**c**, **d**). (**a**, **c**) lower magnification HAADF images; (**b**, **d**) higher magnification EDS maps showing similar precipitation behavior in both specimens. Adapted with permission from Ref. [112]

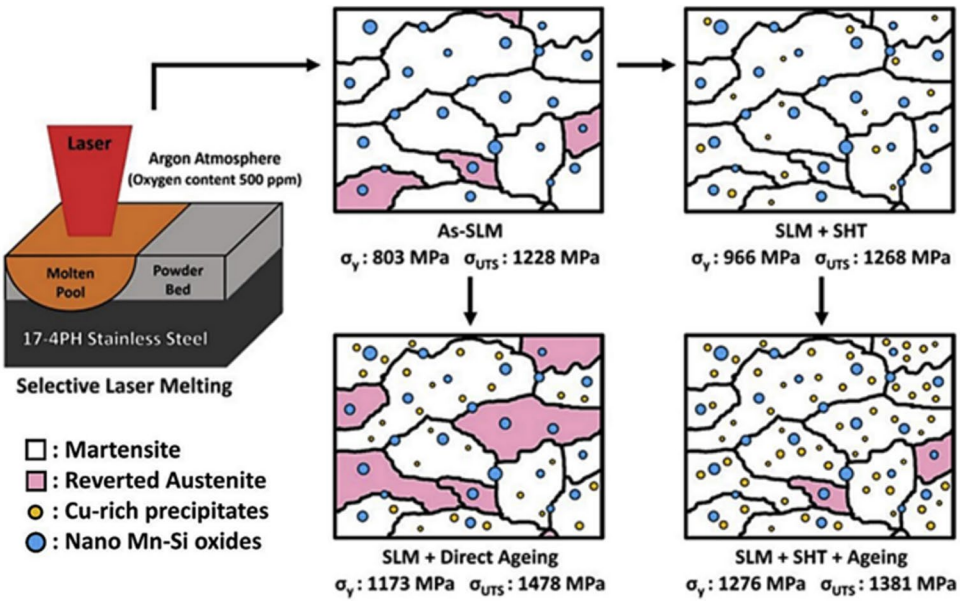

Fig. 16 Schematic representation of microstructure-property correlation of SLM processed 17–4 PH. Reprinted with permission from Ref. [115]

inclusions. However, elongation at failure after the same heat treatment is usually lower than that of wrought-aged counterparts due to early fracture from embedded porosity [128]. Li et al. [114] successfully obtained mechanical properties of SLM-manufactured 17–4 PH comparable to traditionally wrought material by tuning the homogenization heat treatment. A Solution heat treatment at 1150 °C for one hour and aging at 482 °C for one hour resulted in the best trade-off between strength and ductility, with an elongation of 10.5% and an UTS of 1399 MPa (vs. 9% and 1379 MPa for wrought aged 17-4PH). Several researchers investigated the direct aging of SLM-processed PH SSs without prior solution heat treatment [113, 115, 128, 129]. It has been observed that direct-aged samples show a slight increase in strength and hardness and a pronounced work hardening capacity due to the high fraction of the retained austenite and limited precipitation hardening [115]. Over-aging (H1150) increases ductility and reduces strength and hardness owing to the combined effect of coarsened Cu-precipitates and increased retained austenite [130]. Very limited works are performed on the response of SLMed PH SSs to the HIP process. In a recent study, Shi et al. [131] conducted four different sets of HIP experiments referred to as HIP-SHT, HIP-A, HIP-B, and HIP-C (see Fig. 17a–d). All samples were solution-treated at 1040 °C for two hours under 150 MPa pressure. HIP-SHT, HIP-A, and HIP-C specimens were cooled using the uniform rapid quenching mode (URQ). HIP-C samples underwent a slow controlled cooling. No subsequent aging was done on HIP-SHT. Whereas, HIP-A and HIP-C samples were aged at 480 °C for four hours under pressure above 100 MPa, followed by URQ cooling. For HIP-B samples, the aging treatment at 480 °C for four hours was conducted in a furnace under vacuum conditions, followed by water cooling. The mechanical testing results indicated that solutionizing and aging done under HIP, followed by URQ (HIP-A) simultaneously improved tensile strength by 6% and ductility by 37% compared to the as-build condition. The elimination of internal defects and the rapid cooling of URQ preventing the coarsening of grains and precipitates explain these results. The combination of HIP solutionizing, followed by URQ, and subsequent vacuum aging, followed by water quenching (HIP-B), has significantly enhanced the tensile strength from 906 MPa (for as-built sample) to 1440 MPa while maintaining same ductility (Fig. 17e).

4.2.3 Fatigue properties of martensitic PH SSs processed by SLM

A Few studies investigated the fatigue performance of SLM-fabricated 17–4 PH and 15–5 PH. The results indicated that the presence of process-induced defects such as lack of fusion, pores, and surface roughness is detrimental to fatigue life, resulting in lower fatigue strength compared to wrought material. Yadollahi et al. [120] and Sarkar et al. [132] investigated the effects of building orientation and different heat treatments on 17–4 PH and 15–5 PH, respectively. Building orientation was found to have a significant influence on fatigue properties. The lower fatigue strength of the vertically built specimens was mainly attributed to the higher stress concentration of defects perpendicular to the loading axis [132]. Solution annealing and subsequent peak aging were beneficial for low cycle fatigue (LCF) but detrimental for high cycle fatigue (HCF) of PH SSs. This was ascribed to aged specimens becoming brittle and

Table 4 Mechanical properties of martensitic PH stainless steels fabricated by SLM

Grade	Equipment	Condition	BD	austenite volume fraction [%]	Ys [MPa]	References
17–4 PH	EOS M270	600 °C/2 h	–	72	600	[119]
17–4 PH	EOS M270	788 °C/1 h	H	–	610	[88]
			I		737	
17–4 PH	EOS M280	AB	H	36	661	[128]
		H900		40.5	945	
		H1025		10.4	870	
		H1150		5.6	1005	
		CA		0	939	
		CA-H900		3.3	1352	
		CA-H1025		4.7	1121	
		CA-H1150		20.7	859	
17–4 PH	EOS M270	AB	–	50	570	[111]
		650 °C/2 h		–	619	
		788 °C/2 h		–	857	
		788 °C/2 h + H900		–	1126	
17–4 PH	Self-developed machine	AB	–	–	625.5	[172]
		CA-H1025			1028.7	
17–4 PH	EOS M280	AB	H	–	784	[114]
		1150 °C/0.5 h + H900			1130	
		1150 °C/1 h + H900			1280	
		1150 °C/4 h + H900			1309	
		1150 °C/8 h + H900			1165	
17–4 PH	Self-developed machine	AB	H	6.2	803	[115]
		788/2 h		1.5	966	
		788/2 h + H900		5	1276	
		H900		17.9	1173	
17–4 PH	ProX 100	AB	V	3	580	[120]
			H	7	650	
		CA-H900	V	–	1020	
			H	–	1250	
15–5 PH	EOS M290	AB	V	10	–	[113]
			H	9.6		
		CA	V	–		
			H			
		CA-H900	V	–		
			H			
		H900	V	18.6		
			H	15.4		
15–5 PH	EOS M270	H900	V	–	1100	[173]
			H		1297	
15–5 PH	EOS M270	AB	H	13	1050	[130]
		CA-H900			1300	
		CA-H1150			950	
15–5 PH	SLM Solutions	AB	–	10.8	625	[127]
		CA-H900		1.92	1317	
15–5 PH	HBD-280	AB	H	16.31	944	[105]

Standard reference values

Grade	Condition	YS [MPa]	UTS [MPa]	El. [%]	H [HRC]	References
17–4 PH	CA-H900	1170	1310	10	40	[174]
15–5 PH	CA-H900	1170	1310	10	40	[174]

AB As-built state, *CA* Condition A state (≈1050° C for 0.5h followed by air or water-quenching); CA-H900 (condition A + aging at 482° C for one hour); H900 (direct aging at 482 °C for one hour); H1025 (aging at 550 °C for four hours); H1150 (aging at 620 °C for four hours)

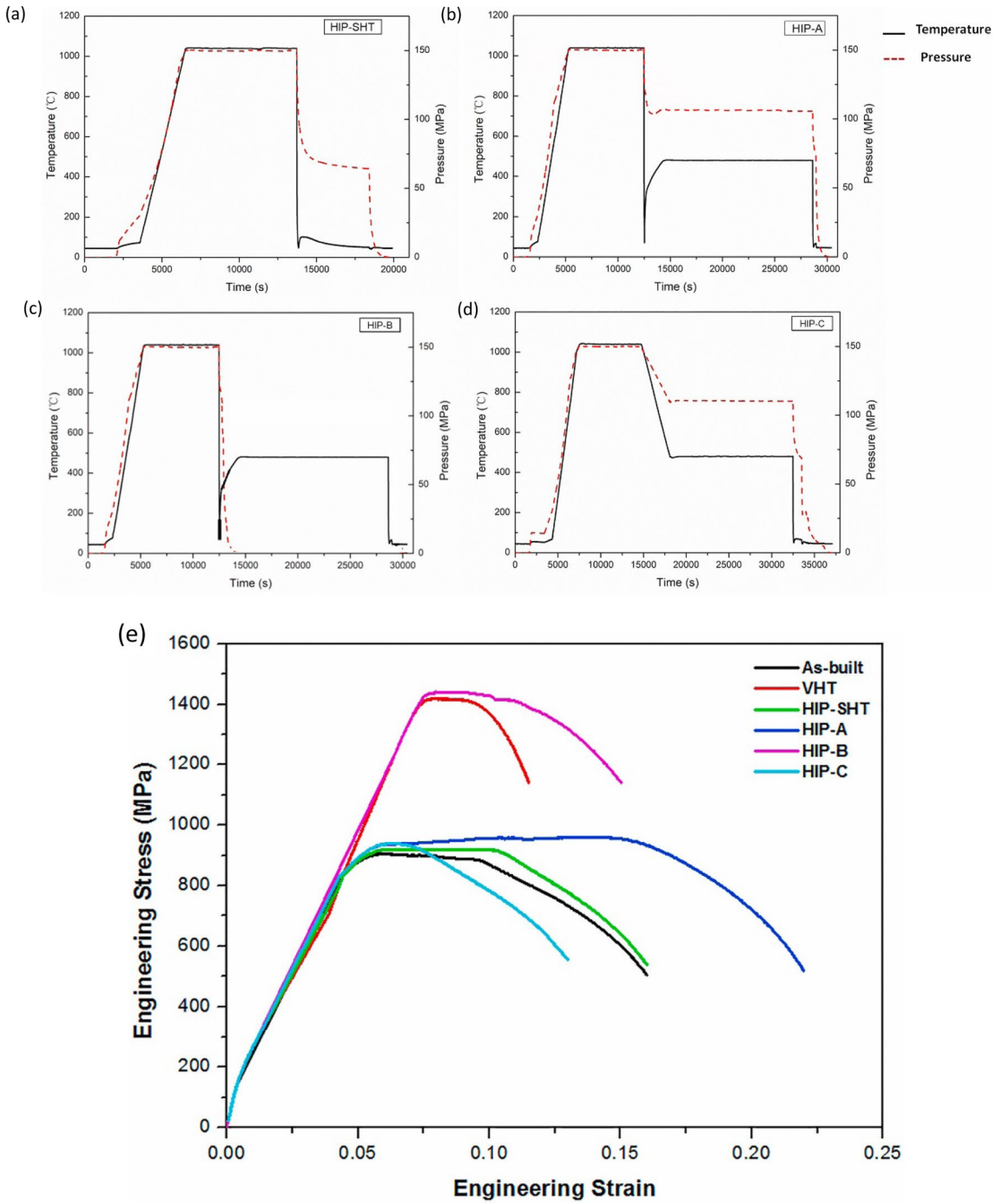

Fig. 17 Effect of HIP on SLMed 17-4PH Stainless steel: **a**–**d** HIP treatment profiles of the conducted experiments **b** Stress–strain curves of the as-built, vacuum (VHT) and HIP heat-treated specimens. Adapted with permission from Ref. [131]

more sensitive to defects in HCF, where the crack initiation governs the fatigue life [120]. In contrast, overaging made specimens more ductile and improved fatigue strength under cyclic loading through coarsening Cu-precipitates and increasing retained austenite. Nezhadfar et al. [133] investigated the effect of the shield gas as an in-situ process defect-structure refiner on fatigue behavior of SLM 17 – 4 PH SS. They demonstrated enhanced crack growth resistance and axial fatigue properties in the HCF for samples built under nitrogen as a shielding gas. The reason for this improvement is the finer microstructure, smaller defect size, and higher retained austenite fraction obtained under the N_2 atmosphere compared to Argon. According to the reported studies, proper selection of build orientation, shielding gas,

and post-treatment can considerably reduce sensitivity to defects of SLM PH SSs and improve fatigue performance under HCF.

4.2.4 The Corrosion Resistance of SLM-Processed Martensitic PH SSs

According to the existing literature, SLM-fabricated 15–5 PH and 17–4 PH showed greater resistance to corrosion than wrought material [134–137]. Irrinki et al. [136] found that full-dense samples from gas-atomized and water-atomized 17–4 PH powders exhibited higher polarization resistance than the wrought sample. A recent study on the electrochemical behavior of SLM-processed 17–4 PH revealed a higher resistance to localized corrosion and pitting in 0.1 M NaCl solution and a more stable passive film compared to wrought material [135]. This improvement in the corrosion performance was related to the refined microstructure with homogenously distributed NbC precipitates and the retained austenite enriched in nitrogen, which is known to have a beneficial influence on corrosion resistance [134, 135]. Wang et al. [137] proved that retained austenite at the melt pool boundaries of SLM-built 15–5 PH has a higher surface potential than martensite. Thus, samples that were directly aged (i.e., with a higher fraction of retained austenite) showed higher pitting potential and improved passive behavior compared to samples that were solutionnized before aging. Controversially, Sarkar et al. [129] investigated the effect of different heat treatments on the SLM 15–5 PH pitting corrosion of and found that samples aged without solution annealing corrode more than the samples aged after annealing. This was attributed to the higher amount of chromium carbides in directly aged samples. Therefore, the corrosion performance of PH stainless steels needs to be more deeply elucidated in the future, since corrosion resistance is the primary characteristic of using stainless steels in various applications.

4.2.5 Selective laser melting of 420 martensitic stainless steel

420 stainless steel is widely used in tooling applications such as injection molds due to its high strength, hardness and corrosion resistance. In the last decade, a growing interest has been addressed to SLM processed 420 stainless steel to take advantage of its geometrical flexibility. Zhao et al. [106] investigated the effect of process parameters on phase composition, density, and hardness of SLM 420. They claimed that it could meet the requirements of injection mold application with a relative density of 99% and a hardness of 50.7 HRC. Krakhmalev et al. [138] demonstrated that thermal cycling caused in-situ partitioning and austenite reversion, resulting in a thermally decomposed martensite and a high amount of austenite. A few studies investigated the microstructure and mechanical properties of SLM-fabricated 420 [107, 139, 140]. Despite the phase composition being a mixture of austenite and martensite, promising tensile strength and hardness are obtained, surpassing those of conventional material. The reported UTS is 1000–1697 MPa and elongation is 2.5%–9.7% in the as-built condition. Low-temperature tempering was found to improve yield strength, tensile strength, and elongation while maintaining good hardness (> 50 HRC) [107]. The fine microstructure with sub-micron martensite needles, the austenite formation, and the transformation-induced plasticity (TRIP) were the reason for these results [139].

4.3 Duplex Stainless Steels

Duplex stainless steels (DSS) are a subgroup of the stainless-steel family. These are referred to as duplex grades because their metallurgical structure is composed of two phases, austenite and ferrite, in about equal proportions. The high chromium concentration provides high corrosion resistance [141], the austenite phase contributes to toughness, whereas ferrite enhances strength [142]. Bi-phase steels have greater ductility than ferritic stainless steels and greater strength and welding capability than austenitic stainless steels. DSS exhibits superior corrosion resistance over mono-phase stainless steels, mainly due to Cr and Mo presence [142–144].

Duplex stainless steel has a reduced molybdenum and nickel content, which makes it more affordable [32]. Duplex stainless steel can be utilized in various applications, including chemical processing, oil and gas pipelines for production and transmission, and offshore oil and gas drilling and exploration [145]. The application generally competes with higher alloy austenitic grades in harsh environmental conditions with significant mechanical loads.

Publications regarding SLM of DSS grades are pretty limited. SAF 2205 and SAF 2507 are the most commonly studies DSS; their chemical compositions are given in Table 5. Fatigue properties are not reported since no data are available in the literature in this field.

4.3.1 As-Built Microstructure of SLM-Processed Duplex Stainless Steel

According to the SLM process parameters, the morphological and crystallographic texture as well as the average grain size are significantly impacted by the laser power, scanning speed, and volumetric energy density [146]. Saeidi et al. [142] reported a macro-textured mosaic structure with square-like grains in SLM-processed SAF2507. However, UNS S31803

(SAF 2205) DSS exhibits a columnar grain morphology oriented toward the building direction, which corresponds to the maximum heat flux toward its base plate [145, 147]. These long grains spread across several layers, show that epitaxial grain growth is taking place. However, the epitaxial microstructure is often slowed down at the solidification front by a new grain with random crystallographic orientations, which leads to a more isotropic microstructure [145]. For the as-built state, the temperature gradient and solidification velocity resulted in an entirely ferritic phase [142, 145, 147]. As in welding, the rapid cooling rate of 10^4 K/s to 10^6 K/s in SLM results in a complete primary solidification of delta ferrite. Furthermore, austenite and subsequent precipitations are almost entirely suppressed in the as-built state [148]. Mirz et al. [149] investigated the effect of building chamber atmosphere on the phase composition of DSS. No substantial differences were observed in the as-built microstructure. Both argon and nitrogen atmosphere resulted in a fully ferritic structure. A high dislocation density is typically observed, like in other metals processed by SLM. It could be justified by quick solidification and self-quenching [142, 145, 150]. In addition to the dislocation loops, chromium nitrides and isothermal nitrides have been seen in the grain interior. The chromium nitrides are believed to develop straight from the melt pool, also known as quenched-in-nitrides, because of nitrogen's higher solubility in austenite than in ferrite, at high cooling rates. Nitrogen has insufficient time to diffuse or contribute to any austenite stabilization; as a result, some nitrogen forms the nitride phase. The isothermal nitride results from the intrinsic heat treatment due to the thermal cycling during the SLM process. In addition, refined secondary austenite grains form at grain boundaries due to this annealing effect. Secondary austenite and the sigma phase develop from delta ferrite in the following sequence: $\delta \rightarrow \gamma_2 + \sigma$ [142, 145].

When it comes to comparing conventional DSS with SLM-processed ones, in conventional DSS, austenite nucleation occurs by static or dynamic recrystallization of the ferritic matrix [151, 152]. An annealing heat treatment can alter the phase composition and redistribute alloying elements between the ferrite and austenite phases [153]. However, in the as-built condition of the SLM-manufactured DSS, austenite production is virtually wholly suppressed because of process-related high cooling rates [142, 145].

4.3.2 Microstructure of SLM-Processed Duplex Stainless Steel After Heat Treatment

Annealing is a frequent post-treatment for duplex stainless steel. Additionally, studies indicate that the as-built DSS has a pure ferritic phase and that the ferrite/austenite phase ratio can reach a value extremely near to one upon annealing [154–156]. Several heat treatments at temperatures ranging from 900 to 1200 °C for 5 min each were used to achieve the required austenitic-ferritic microstructure. The high dislocation density of the as-built microstructure promoted a complete recrystallization following heat treatment, based on the formation and motion of high-angle grain boundaries. Recrystallization is also determined by the considerable shift in crystallographic and morphologic orientation of the microstructure [145]. In SLMed specimens, similar to standard duplex stainless steel, secondary austenite nucleation occurs during annealing and the formation is temperature-dependent. When annealing is performed at a lower temperature (about 900 °C), fine intergranular secondary austenite regions form in the ferritic matrix due to ferrite stabilising elements such as Cr and Mo being bonded by intermetallic phases such as carbides or nitrides [143, 144]. Secondary austenite occurs near ferritic grain boundaries at higher annealing temperatures (about 1200 °C). At this temperature, a coarse-grained delta ferritic microstructure forms; then, secondary austenite nucleates only at recrystallized delta ferritic grain boundaries. Annealing at 1000 °C resulted in the greatest volume fraction of austenite of 34%. This volume decreases when the annealing temperature is increased or decreased (see Fig. 18) [143, 145]. Papula et al. [147] found that maximal austenite fraction (46,4 vol%) occurs at high annealing temperatures in the range of 1000–1050 °C for longer annealing time (60min) for the 2205 DSS grade. Annealing reactivates the metastable ferrite to austenite transition inhibited by rapid cooling. It has been found that increased annealing temperature results in the evolution of more metastable ferrite into austenite, whereas thermodynamic equilibrium promotes the transformation of austenite into ferrite [147]. Annealing of SLM-fabricated UNS S32707 at a temperature range of 1050–1200 °C for one hour indicates that a good balance between the two phases could be reached at 1100°C. As the temperature increases, the ferrite phase percentage increases from 59.5 to 63.4% for 1100 and 1200 °C, respectively [157].

Table 5 Chemical composition of duplex stainless steels commonly used in SLM [167]

Grade name	Chemical composition (%w)										
	Fe	Cr	Ni	Mo	Mn	Si	C	S	P	N	Cu
2205 (S32205/31803)	Bal	22	5	3.2	≤2.0	≤1.0	≤0.03	≤0.015	≤0.03	0.18	–
2507 (S3270)	Bal	25	7	4	≤1.2	≤0.8	≤0.03	≤0.015	≤0.025	0.3	0.5

4.3.3 Tensile Behavior of Duplex Stainless Steel

Tensile tests show that heat treatment significantly affects the final mechanical response. When compared to heat-treated specimens, the nearly complete ferritic as-built specimens have a higher ultimate tensile strength and a lower elongation at fracture [147], as can be seen in Fig. 19. This behavior could be explained by nitride precipitation as well as nano-sized dislocations in as-built specimens that hinder dislocation movement, resulting in higher strength. Different crystalline grain orientations, boundary impurities, and precipitates prevent slip/slide effects [142]. The best combination of strength and elongation was obtained after annealing at 1000 °C [145]. When compared to the conventionally produced material with a similar chemical composition, the SLM-processed and heat-treated 2205 DSS had significantly higher microhardness (255–280 HV1), yield strength (520–560 MPa), and tensile strength (810–870 MPa), while uniform elongation was in a similar range (23–25 percent) [147]. SLM-processed UNS S32707 DSS grade showed the best comprehensive mechanical properties after annealing at 1150°. The measured tensile strength, yield strength, elongation, section shrinkage, microhardness, and impact absorption energy, in this condition, were 901 MPa, 658 MPa, 36.4 percent, 48.4 percent, 291.5 HV, and 132 J, respectively [157]. In a recent study [158], the addition of minor in-situ Ti additions to S2205 DSS resulted in the formation of nano-inclusions. These nano-inclusions played a key role in refining the microstructure by impeding the movement of austenite/ferrite interfaces during annealing after SLM. Additionally, they contributed significantly to a precipitation-strengthening increment. The resulting DSS, enhanced by these nano-inclusions, displayed impressive mechanical properties, boasting a tensile strength of around 910 MPa and a total elongation of approximately 52%. In comparison, the commercial counterpart exhibited a lower tensile strength of approximately 610 MPa and an elongation of around 45%. According to [149], hot isostatic pressing significantly influences tensile behavior, as it reduces the porosity of SLM specimens. The ultimate tensile strength

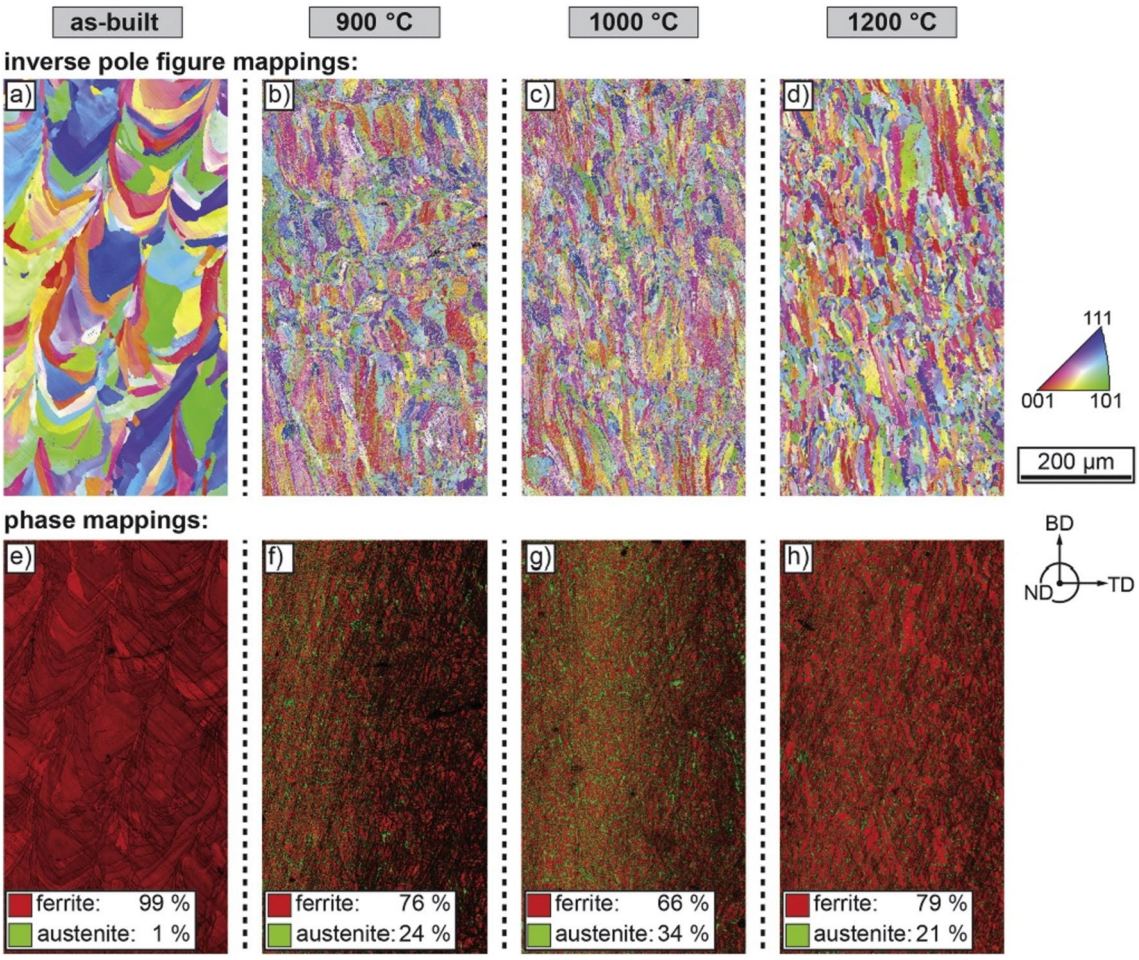

Fig. 18 EBSD maps: **a**–**d** inverse pole figure maps, **e**–**h** corresponding phase maps of the as-built and solution-annealed samples, showing the evolution of the austenite phase with heat treatment temperature. Reprinted with permission from Ref. [145]

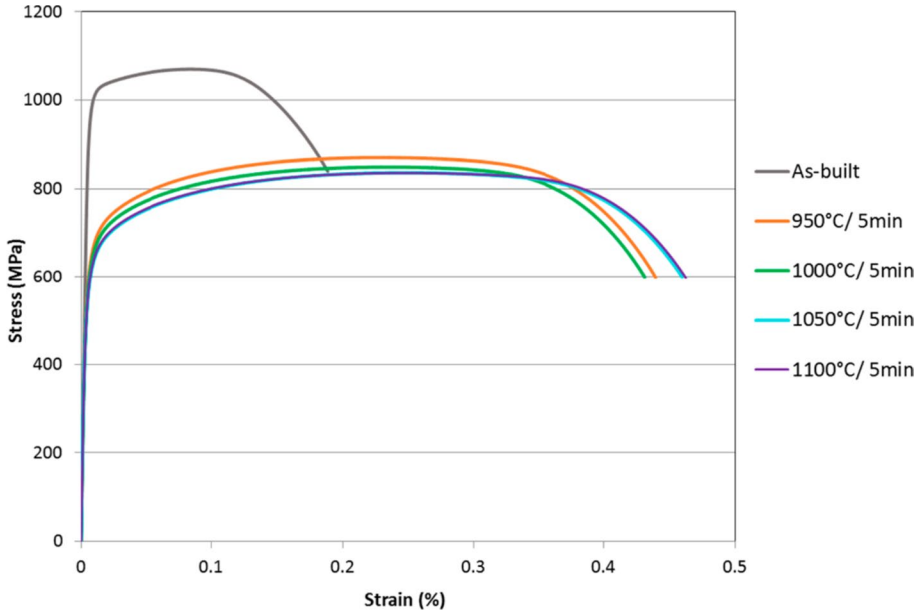

Fig. 19 Stress-stain curve for 2205 DSS processed by SLM in the as-built and annealed conditions. Reprinted from Ref. [147]

increased to 724.9 MPa by HIP post-treatment followed by solution annealing at 1080 °C for 60 min, while the value for the only annealed sample is 692.2 MPa.

4.3.4 Corrosion Behavior

The results of a study on the effect of building direction and annealing on SLM-processed 2205 Duplex stainless steel indicate that the build orientation and annealing were not as important as the chemical composition in predicting passivity and pitting resistance [154]. In contrast, Papula et al. [147] observed that annealing heat treatment increased the pitting corrosion resistance of the as-built SLM-processed material. The study of annealing temperatures (1050–1200 °C) on UNS S32707 grade reveals that pitting resistance for as-built material would be improved in the annealing solution, with the maximum pitting resistance occurring at 1100 °C [157].

4.4 Ferritic Stainless Steels

Ferritic stainless steel refers to the class of stainless alloys with chromium concentration between 10.5 and 30% and less than 0.20% carbon. These allays are not heat treatable, cold rolling is the only hardening method [31]. Thanks to their superior chloride stress-corrosion resistance, smaller linear expansion, higher thermal conductivity, and lower cost compared to austenitic stainless steel, ferritic stainless steel is frequently used in construction [159] and in safety-related applications such as reactor pressure vessels, steam generators, valves, and pipes [160].

Oxide dispersion strengthened (ODS) steels are ferritic stainless steels that contain a fine dispersion of Y, Ti, and Nb oxides in the ferritic matrix, improving their high-temperature strength and creep strength [161]. They are used for high-temperature applications such as turbine blades and heat exchanger tubing [162]. ODS steels are usually processed using powder metallurgy methods. Stainless steel powder is mechanically alloyed with oxide powder. The powder mixture is then consolidated by HIP or hot extrusion [160]. Since their conventional processing is complicated, the production of ODS using the SLM process is attracting the interest of researchers. However, the use of ferritic stainless steels in the SLM process is still in its early stages, with few available studies on the topic. PM2000 alloy and FeCrAl are common ODS alloys used in AM [163].

4.4.1 Microstructure of Ferritic Stainless Steels

The microstructural evolution of ferritic stainless steels at various process parameters during the SLM process has received little attention. A study by Jiang et al. [159] investigates ferritic stainless steel's microstructure, microhardness, and corrosion behavior by varying laser power, scan speed and hatching distance. The as-built microstructure comprised α-Fe and a small amount of $Cr_{23}C_6$. A cellular morphological structure was visible in the microstructure of the SLM specimens with a random crystallographic texture. Scanning speed significantly affected microstructure; its increase resulted in finer grain size, a smaller amount of $Cr_{23}C_{6,}$ a larger proportion of LAGBs, and a higher dislocation density. Karlsson et al. [162] compared SLM-produced 441 ferritic stainless steel with its cast and hot-rolled counterpart. A significant difference was observed with an anisotropic and finer microstructure containing Ti and O-rich precipitates.

In contrast, cast and hot-rolled samples showed coarser grains with TiN and Nb (C, N) precipitates. Similar precipitation behavior was observed in SLM-fabricated Fe-14Cr ODS SS, where only Y–Ti-O was kept without carbides, titanium or aluminum oxides, typically present in conventional ODS SSs [160]. However, the SLM-built microstructure in this study was coarser than that of conventional ODS.

4.4.2 Mechanical Properties of SLM-Processed Ferritic Stainless Steels

Very limited data is available in the literature about the mechanical properties of ferritic stainless steels. Boegelein et al. [164] investigated the tensile properties of thin-walled builds made of SLM-processed ODS-PM2000. They showed that post-build annealing at 1200 °C for 1 h improved the yield strength, comparable to that of conventional material.

Another study comparing SLM ferritic stainless steel SS441 to hot-rolled alloy demonstrates improved mechanical properties of SLM-printed material, with more than 30 times higher impact energy. The enhanced mechanical properties of the SLMed sample were attributed to a smaller grain size, which resulted in a greater Hall–Petch strength. The results proved definitively that SLM is a viable manufacturing process for ferritic stainless steels with increased strength [162]

5 Summary and outlook

Stainless steels are in high demand in almost all industrial sectors due to their widespread supply chain, non-reactive nature, and relatively low cost. Therefore, their use in additive manufacturing is receiving significant attention. Selective laser melting is one of the most popular and fastest-growing additive manufacturing technologies. This review underlines the potential of the SLM process to produce fully dense near-net-shape parts with promising properties using different grades of stainless steel. These achievements, along with SLM's abilities to produce customized components, complex geometries, and lightweight structures, contribute to the wide adoption of the SLM process in stainless steel production. The published research on SLM of stainless steel reflects the opportunities and challenges of this processing route. Diverse stainless-steel grades belonging to different classes (i.e., austenitic, martensitic, precipitation hardening, and duplex) have been addressed in the literature, with the majority of papers focused on 316L austenitic stainless steel. The following is a summary of the most important findings from the extant literature on SLM of stainless steels:

- Defect-free parts made from stainless steel can be processed routinely using optimized process parameters. Less than 0.1% of porosity can exist without detrimental effect on monotonic and cyclic mechanical behavior.
- SLM process's fast-cooling rate and directional temperature gradient result in a hierarchical microstructure with a considerable volume fraction of nano-inclusions and a strong crystallographic < 100 > texture along the building direction.
- For martensitic, precipitation hardening, and duplex stainless steels, significant changes are observed in the phase composition of the SLM-built microstructure compared to the conventional materials. This is mainly attributed to the high cooling rate, which may alter the primary solidification mode and make solid-state phase transformations unachievable or incomplete. A heat treatment is usually required to achieve the intended microstructure.
- SLM-produced stainless steels typically exhibit comparable or even higher hardness and tensile strength than those of conventionally processed counterparts due to the fine grain size, hierarchical microstructure features and ODS effect of nano-inclusions. Although ductility seems negatively affected by process-induced porosity, suitable combinations of strength and ductility have been achieved either by in-situ tailored microstructure or by post-heat treatment.
- Being brittle, thus, more sensitive to defects under cycling loading, martensitic PH SSs showed poor fatigue properties. Whereas SLM austenitic stainless steel had more defect-tolerant behavior, resulting in satisfactory fatigue resistance thanks to their ductility. Reducing sensitivity to defects involves the appropriate selection of the build strategy and the building orientation to avoid defects being perpendicular to the loading axis under HCF. Combining and optimizing post-treatment techniques such as surface finishing, HIP and heat treatment would improve fatigue performance by reducing defects and increasing ductility leading to a better resistance for crack initiation and propagation under cyclic loading.
- The Corrosion resistance of SLM-fabricated stainless steels is generally better than that of conventionally produced material. However, the mechanisms behind these enhanced properties are poorly addressed in the literature and need to be clarified in the future.

Despite the significant effort that has been undertaken in the field of SLM of stainless steel so far, several challenges still need to be addressed. These challenges define the path for further research and exploitation. Moving forward, possible directions to tackle some common research gaps in SLM of stainless steel may include:

- Alloy optimization: Despite their popularity in additive manufacturing, a very narrow group of stainless steels is commonly printed today compared to the vastness of

stainless steel currently processed by traditional manufacturing techniques. Researchers have to investigate and optimize the alloy compositions of stainless steels for SLM by fine-tuning alloying elements to enhance printability, reduce defects, and improve mechanical properties.

- Powder quality: Addressing issues such as powder oxidation and contamination and analyzing the influence of powder characteristics on the final part quality are essential to researching and developing high-quality powders.
- Parameters optimization: The high divergence of SLM-produced stainless steel properties reflects a lack of control over the attained microstructure. Conducting systematic studies to optimize process parameters for different stainless-steel alloys while considering the interaction between parameters and their impact on part quality can provide a deeper understanding of the process-structure–property relationships.
- In-situ monitoring: Real-time monitoring can help in identifying issues and improving part quality. Thus, it is important to develop, implement, and enhance in-situ monitoring techniques to detect and mitigate defects during the printing process to achieve the progression of SLM as a single-step process with reduced production time and cost.
- Multi-physics modeling: multi-physics models to simulate the complex interactions between thermal, fluid, and mechanical aspects of the SLM process should be enhanced.
- Heat treatment strategies: Standard heat treatments are not designed for SLM-processed stainless steels. Thus, upcoming studies should consider exploring innovative heat treatment methods by changing heat treatment parameters and conditions to reduce residual stresses, control microstructure, and enhance the mechanical properties of SLM-printed stainless steels.
- Post-processing techniques: The investigation and optimization of post-processing techniques such as HIP and surface finishing could help improve fatigue performance.
- Standardization: Future research work should contribute to the development of standards for SLM of stainless steels. Standardized testing methods and quality assurance protocols can help ensure the reliability and repeatability of the process.
- Case Studies and Applications: Researchers have to collaborate more with industry partners to apply SLM-printed stainless steel components in real-world applications. This can provide valuable insights into the performance and reliability of printed parts, validate research findings, and facilitate technology transfer.
- Environmental Impact Assessment: More attention should be given to the sustainability of the SLM process by conducting thorough life cycle assessments to evaluate the environmental impact of SLM-printed stainless steels compared to traditional manufacturing processes.

These steps will pave the way toward the advancement of knowledge in the SLM of stainless steels, bridging existing gaps, and contributing to a more efficient, reliable, and sustainable manufacturing process.

Declarations

Conflict of interest The authors declare that they have no known competing financial interests or personal relationships that could have appeared to influence the work reported in this paper.

References

1. W.E. Frazier, J. Mater. Eng. Perform. **23**, 1917–1928 (2014). https://doi.org/10.1007/s11665-014-0958-z
2. D. Herzog, V. Seyda, E. Wycisk, C. Emmelmann, Acta Mater. **117**, 371–392 (2016). https://doi.org/10.1016/j.actamat.2016.07.019
3. T.J. Horn, O.L.A. Harrysson, Sci. Prog. **95**, 255–282 (2012). https://doi.org/10.3184/003685012x13420984463047
4. J. Spallek, D. Krause, Procedia CIRP **50**, 281–286 (2016). https://doi.org/10.1016/j.procir.2016.05.022
5. T. DebRoy, H. Wei, J. Zuback, T. Mukherjee, J. Elmer, J. Milewski, A.M. Beese, A. Wilson-Heid, A. De, W. Zhang, Prog. Mater. Sci. **92**, 112–224 (2018). https://doi.org/10.1016/j.pmatsci.2017.10.001
6. R. Swetha, L. Siva Rama Krishna, B. Hari Sai Kiran, P. Ravinder Reddy, S. Venkatesh, Mater. Today: Proc. **62**, 4332–4340 (2022). https://doi.org/10.1016/j.matpr.2022.04.840
7. C.Y. Yap, C.K. Chua, Z.L. Dong, Z.H. Liu, D.Q. Zhang, L.E. Loh, S.L. Sing, Appl. Phys. Rev. **2**, 041101 (2015). https://doi.org/10.1063/1.4935926
8. J.J. Beaman, D.L. Bourell, C.C. Seepersad, D. Kovar, J. Manuf. Sci. Eng. **142**, 110812 (2020). https://doi.org/10.1115/1.4048193
9. I. Yadroitsev, I. Smurov, Phys. Procedia **5**, 551–560 (2010). https://doi.org/10.1016/j.phpro.2010.08.083
10. A. Mostafaei, C. Zhao, Y. He, S. Reza Ghiaasiaan, B. Shi, S. Shao, N. Shamsaei, Z. Wu, N. Kouraytem, T. Sun, J. Pauza, J.V. Gordon, B. Webler, N.D. Parab, M. Asherloo, Q. Guo, L. Chen, A.D. Rollett, Curr. Opin. Solid State Mater. Sci. **26**, 100974 (2022). https://doi.org/10.1016/j.cossms.2021.100974
11. M. Anand, A.K. Das, Opt. Laser Technol. **139**, 106914 (2021). https://doi.org/10.1016/j.optlastec.2021.106914
12. Z. Snow, A.R. Nassar, E.W. Reutzel, Addit. Manuf. **36**, 101457 (2020). https://doi.org/10.1016/j.addma.2020.101457
13. J.H. Tan, W.L.E. Wong, K.W. Dalgarno, Addit. Manuf. **18**, 228–255 (2017). https://doi.org/10.1016/j.addma.2017.10.011
14. U. Scipioni Bertoli, A.J. Wolfer, M.J. Matthews, J.P.R. Delplanque, J.M. Schoenung, Mater. Des. **113**, 331–340 (2017). https://doi.org/10.1016/j.matdes.2016.10.037
15. S. Liu, H. Guo, Materials **13**, 3632 (2020). https://doi.org/10.3390/ma13163632

16. D. Gu, Y. Shen, Mater. Des. **30**, 2903–2910 (2009). https://doi.org/10.1016/j.matdes.2009.01.013
17. R. Li, J. Liu, Y. Shi, L. Wang, W. Jiang, Int. J. Adv. Manuf. Technol. **59**, 1025–1035 (2012). https://doi.org/10.1007/s00170-011-3566-1
18. J.P. Kruth, L. Froyen, J. Van Vaerenbergh, P. Mercelis, M. Rombouts, B. Lauwers, J. Mater. Process. Technol. **149**, 616–622 (2004). https://doi.org/10.1016/j.jmatprotec.2003.11.051
19. Y. Liu, Y. Yang, D. Wang, Int. J. Adv. Manuf. Technol. **87**, 647–656 (2016). https://doi.org/10.1007/s00170-016-8466-y
20. C. Li, J.F. Liu, Y.B. Guo, Procedia CIRP **45**, 171–174 (2016). https://doi.org/10.1016/j.procir.2016.02.058
21. P. Mercelis, J.-P. Kruth, Rapid Prototyp. J. **12**, 254–265 (2006). https://doi.org/10.1108/13552540610707013
22. M.F. Zaeh, G. Branner, Prod. Eng. Res. Devel. **4**, 35–45 (2010). https://doi.org/10.1007/s11740-009-0192-y
23. A.S. Wu, D.W. Brown, M. Kumar, G.F. Gallegos, W.E. King, Metall. Mater. Trans. A **45**, 6260–6270 (2014). https://doi.org/10.1007/s11661-014-2549-x
24. M. Ghasri-Khouzani, H. Peng, R. Rogge, R. Attardo, P. Ostiguy, J. Neidig, R. Billo, D. Hoelzle, M. Shankar, Mater. Sci. Eng. A **707**, 689–700 (2017). https://doi.org/10.1016/j.msea.2017.09.108
25. J.-P. Kruth, J. Deckers, E. Yasa, R. Wauthlé, Proc. Inst. Mech. Eng. Part B J. Eng. Manuf. **226**, 980–991 (2012). https://doi.org/10.1177/0954405412437085
26. T. Peng, K. Kellens, R. Tang, C. Chen, G. Chen, Addit. Manuf. **21**, 694–704 (2018). https://doi.org/10.1016/j.addma.2018.04.022
27. Y. Wang, T. Peng, Y. Zhu, Y. Yang, R. Tang, Procedia CIRP **90**, 220–225 (2020). https://doi.org/10.1016/j.procir.2020.01.095
28. R. Huang, M. Riddle, D. Graziano, J. Warren, S. Das, S. Nimbalkar, J. Cresko, E. Masanet, J. Clean. Prod. **135**, 1559–1570 (2016). https://doi.org/10.1016/j.jclepro.2015.04.109
29. M. Baumers, C. Tuck, R. Wildman, I. Ashcroft, E. Rosamond, R. Hague, in *Proceedings of the 23rd Annual International Solid Freeform Fabrication (SFF) Symposium*, ed. by D.L. Bourell, R.H. Crawford, C.C. Seepersad, J.J. Beaman, H.L. Marcus. Austin, 6-8 August 2012 (University of Texas, Austin, 2012), pp. 932–944
30. R. Huang, M.E. Riddle, D. Graziano, S. Das, S. Nimbalkar, J. Cresko, E. Masanet, J. Ind. Ecol. **21**, S130–S143 (2017). https://doi.org/10.1111/jiec.12641
31. J.R. Davis, *ASM Speciality Handbook Stainless Steels* (ASM International, Materials Park, 1994)
32. M.F. McGuire, *Stainless Steels for Design Engineers* (ASM International, Materials Park, 2008)
33. S. Sun, M. Brandt, M. Easton, in *Laser Additive Manufacturing: Materials, Design, Technologies, and Applications*. ed. by M. Brandt (Woodhead Publishing, 2017), pp.55–77
34. N. Haghdadi, M. Laleh, M. Moyle, S. Primig, J. Mater. Sci. **56**, 64–107 (2021). https://doi.org/10.1007/s10853-020-05109-0
35. K. Abd-Elghany, D. Bourell, Rapid Prototyp. J. **18**, 420–428 (2012). https://doi.org/10.1108/13552541211250418
36. H. Yu, J. Yang, J. Yin, Z. Wang, X. Zeng, Mater. Sci. Eng. A **695**, 92–100 (2017). https://doi.org/10.1016/j.msea.2017.04.031
37. N. Jeyaprakash, C.-H. Yang, K.R. Ramkumar, Met. Mater. Int. **27**, 5179–5190 (2021). https://doi.org/10.1007/s12540-020-00933-0
38. B. Zhang, L. Dembinski, C. Coddet, Mater. Sci. Eng. A **584**, 21–31 (2013). https://doi.org/10.1016/j.msea.2013.06.055
39. C. Qiu, M.A. Kindi, A.S. Aladawi, I.A. Hatmi, Sci. Rep. **8**, 7785 (2018). https://doi.org/10.1038/s41598-018-26136-7
40. D. Wang, C. Song, Y. Yang, Y. Bai, Mater. Des. **100**, 291–299 (2016). https://doi.org/10.1016/j.matdes.2016.03.111
41. E. Liverani, S. Toschi, L. Ceschini, A. Fortunato, J. Mater. Process. Technol. **249**, 255–263 (2017). https://doi.org/10.1016/j.jmatprotec.2017.05.042
42. N. Diaz Vallejo, C. Lucas, N. Ayers, K. Graydon, H. Hyer, Y. Sohn, Metals **11**, 832 (2021). https://doi.org/10.3390/met11050832
43. Y. Zhong, L. Liu, S. Wikman, D. Cui, Z. Shen, J. Nucl. Mater. **470**, 170–178 (2016). https://doi.org/10.1016/j.jnucmat.2015.12.034
44. K. Saeidi, Stainless steels fabricated by laser melting: Scaled-down structural hierarchies and microstructural heterogeneities, Ph.D. Thesis, Stockholm University (2016)
45. T. Kurzynowski, K. Gruber, W. Stopyra, B. Kuźnicka, E. Chlebus, Mater. Sci. Eng. A **718**, 64–73 (2018). https://doi.org/10.1016/j.msea.2018.01.103
46. Z. Sun, X. Tan, S.B. Tor, W.Y. Yeong, Mater. Des. **104**, 197–204 (2016). https://doi.org/10.1016/j.matdes.2016.05.035
47. H. Choo, K.-L. Sham, J. Bohling, A. Ngo, X. Xiao, Y. Ren, P.J. Depond, M.J. Matthews, E. Garlea, Mater. Des. **164**, 107534 (2019). https://doi.org/10.1016/j.matdes.2018.12.006
48. M. Ghayoor, K. Lee, Y. He, C.-H. Chang, B.K. Paul, S. Pasebani, Addit. Manuf. **32**, 101011 (2020). https://doi.org/10.1016/j.addma.2019.101011
49. J. Hou, W. Chen, Z. Chen, K. Zhang, A. Huang, Mater. Sci. Technol. **48**, 63–71 (2020). https://doi.org/10.1016/j.jmst.2020.01.011
50. Z. Zhu, W. Li, Q.B. Nguyen, X. An, W. Lu, Z. Li, F.L. Ng, S.M. Ling Nai, J. Wei, Addit. Manuf. **35**, 101300 (2020). https://doi.org/10.1016/j.addma.2020.101300
51. S. Astafurov, E. Astafurova, Metals **11**, 1052 (2021). https://doi.org/10.3390/met11071052
52. P. Bajaj, A. Hariharan, A. Kini, P. Kürnsteiner, D. Raabe, E.A. Jägle, Mater. Sci. Eng. A **772**, 138633 (2020). https://doi.org/10.1016/j.msea.2019.138633
53. J.W. Fu, Y.S. Yang, J. Alloys Compd. **580**, 191–194 (2013). https://doi.org/10.1016/j.jallcom.2013.05.107
54. K. Saeidi, X. Gao, Y. Zhong, Z.J. Shen, Mater. Sci. Eng. A **625**, 221–229 (2015). https://doi.org/10.1016/j.msea.2014.12.018
55. A. Röttger, J. Boes, W. Theisen, M. Thiele, C. Esen, A. Edelmann, R. Hellmann, Int. J. Adv. Manuf. Technol. **108**, 769–783 (2020). https://doi.org/10.1007/s00170-020-05371-1
56. Y.M. Wang, T. Voisin, J.T. McKeown, J. Ye, N.P. Calta, Z. Li, Z. Zeng, Y. Zhang, W. Chen, T.T. Roehling, Nat. Mater. **17**, 63–71 (2018). https://doi.org/10.1038/nmat5021
57. W.M. Tucho, V.H. Lysne, H. Austbø, A. Sjolyst-Kverneland, V. Hansen, J. Alloys Compd. **740**, 910–925 (2018). https://doi.org/10.1016/j.jallcom.2018.01.098
58. A. Leicht, M. Rashidi, U. Klement, E. Hryha, Mater. Charact. **159**, 110016 (2020). https://doi.org/10.1016/j.matchar.2019.110016
59. F. Yan, W. Xiong, E.J. Faierson, Materials **10**, 1260 (2017). https://doi.org/10.3390/ma10111260
60. M.S. Pham, B. Dovgyy, P.A. Hooper, Mater. Sci. Eng. A **704**, 102–111 (2017). https://doi.org/10.1016/j.msea.2017.07.082
61. P. Krakhmalev, G. Fredriksson, K. Svensson, I. Yadroitsev, I. Yadroitsava, M. Thuvander, R. Peng, Metals **8**, 643 (2018). https://doi.org/10.3390/met8080643
62. H.-Z. Jiang, Z.-Y. Li, T. Feng, P.-Y. Wu, Q.-S. Chen, Y.-L. Feng, L.-F. Chen, J.-Y. Hou, H.-J. Xu, Acta Metall. Sinica **34**, 495–510 (2021). https://doi.org/10.1007/s40195-020-01143-8
63. A. Riemer, S. Leuders, M. Thöne, H.A. Richard, T. Tröster, T. Niendorf, Eng. Fract. Mech. **120**, 15–25 (2014). https://doi.org/10.1016/j.engfracmech.2014.03.008
64. T. Niendorf, S. Leuders, A. Riemer, H.A. Richard, T. Tröster, D. Schwarze, Metall. Mater. Trans. B **44**, 794–796 (2013). https://doi.org/10.1007/s11663-013-9875-z

65. R. Casati, J. Lemke, M. Vedani, Mater. Sci. Technol. **32**, 738–744 (2016). https://doi.org/10.1016/j.jmst.2016.06.016
66. J. Liu, A.C. To, Addit. Manuf. **16**, 58–64 (2017). https://doi.org/10.1016/j.addma.2017.05.005
67. M.L. Montero-Sistiaga, M. Godino-Martinez, K. Boschmans, J.-P. Kruth, J. Van Humbeeck, K. Vanmeensel, Addit. Manuf. **23**, 402–410 (2018). https://doi.org/10.1016/j.addma.2018.08.028
68. J.J. Marattukalam, D. Karlsson, V. Pacheco, P. Beran, U. Wiklund, U. Jansson, B. Hjörvarsson, M. Sahlberg, Mater. Des. **193**, 108852 (2020). https://doi.org/10.1016/j.matdes.2020.108852
69. S.-H. Sun, T. Ishimoto, K. Hagihara, Y. Tsutsumi, T. Hanawa, T. Nakano, Scripta Mater. **159**, 89–93 (2019). https://doi.org/10.1016/j.scriptamat.2018.09.017
70. S. Bahl, S. Mishra, K.U. Yazar, I.R. Kola, K. Chatterjee, S. Suwas, Addit. Manuf. **28**, 65–77 (2019). https://doi.org/10.1016/j.addma.2019.04.016
71. Z. Sun, X. Tan, S.B. Tor, C.K. Chua, NPG Asia Mater. **10**, 127–136 (2018). https://doi.org/10.1038/s41427-018-0018-5
72. E. Tascioglu, Y. Karabulut, Y. Kaynak, Int. J. Adv. Manuf. Technol. **107**, 1947–1956 (2020). https://doi.org/10.1007/s00170-020-04972-0
73. K. Saeidi, X. Gao, F. Lofaj, L. Kvetková, Z.J. Shen, J. Alloys Compd. **633**, 463–469 (2015). https://doi.org/10.1016/j.jallcom.2015.01.249
74. D. Kong, X. Ni, C. Dong, L. Zhang, C. Man, J. Yao, K. Xiao, X. Li, Electrochim. Acta **276**, 293–303 (2018). https://doi.org/10.1016/j.electacta.2018.04.188
75. M. Montero Sistiaga, S. Nardone, C. Hautfenne and J. Van Humbeeck, In Proceedings of the 27th Annual International Solid Freeform Fabrication Symposium-An Additive Manufacturing Conference, (Solid Freeform Fabrication, 2016), pp 558–565
76. E. Liverani, A.H. Lutey, A. Ascari, A. Fortunato, Int. J. Adv. Manuf. Technol. **107**, 109–122 (2020). https://doi.org/10.1007/s00170-020-05072-9
77. N. Ahmed, I. Barsoum, G. Haidemenopoulos, R.A. Al-Rub, J. Manuf. process. **75**, 415–434 (2022). https://doi.org/10.1016/j.jmapro.2021.12.064
78. H.D. Carlton, A. Haboub, G.F. Gallegos, D.Y. Parkinson, A.A. MacDowell, Mater. Sci. Eng. A **651**, 406–414 (2016). https://doi.org/10.1016/j.msea.2015.10.073
79. I. Tolosa, F. Garciandía, F. Zubiri, F. Zapirain, A. Esnaola, Int. J. Adv. Manuf. Technol. **51**, 639–647 (2010). https://doi.org/10.1007/s00170-010-2631-5
80. K. Guan, Z. Wang, M. Gao, X. Li, X. Zeng, Mater. Des. **50**, 581–586 (2013). https://doi.org/10.1016/j.matdes.2013.03.056
81. H. Fayazfar, M. Salarian, A. Rogalsky, D. Sarker, P. Russo, V. Paserin, E. Toyserkani, Mater. Des. **144**, 98–128 (2018). https://doi.org/10.1016/j.matdes.2018.02.018
82. E. Polatidis, J. Čapek, A. Arabi-Hashemi, C. Leinenbach, M. Strobl, Scripta Mater. **176**, 53–57 (2020). https://doi.org/10.1016/j.scriptamat.2019.09.035
83. J.A. Cherry, H.M. Davies, S. Mehmood, N.P. Lavery, S.G.R. Brown, J. Sienz, Int. J. Adv. Manuf. Technol. **76**, 869–879 (2015). https://doi.org/10.1007/s00170-014-6297-2
84. J. Kluczyński, L. Śnieżek, K. Grzelak, A. Oziębło, K. Perkowski, J. Torzewski, I. Szachogłuchowicz, K. Gocman, M. Wachowski, B. Kania, Materials **13**, 3805 (2020). https://doi.org/10.3390/ma13173805
85. O.O. Salman, C. Gammer, A.K. Chaubey, J. Eckert, S. Scudino, Mater. Sci. Eng. A **748**, 205–212 (2019). https://doi.org/10.1016/j.msea.2019.01.110
86. J.J. Lewandowski, M. Seifi, Annu. Rev. Mater. Res. **46**, 151–186 (2016). https://doi.org/10.1146/annurev-matsci-070115-032024
87. J. Suryawanshi, K.G. Prashanth, U. Ramamurty, Mater. Sci. Eng. A **696**, 113–121 (2017). https://doi.org/10.1016/j.msea.2017.04.058
88. T.M. Mower, M.J. Long, Mater. Sci. Eng. A **651**, 198–213 (2016). https://doi.org/10.1016/j.msea.2015.10.068
89. A.B. Spierings, T.L. Starr, K. Wegener, Rapid Prototyp. J. **19**, 88–94 (2013). https://doi.org/10.1108/13552541311302932
90. M. Zhang, C.-N. Sun, X. Zhang, P.C. Goh, J. Wei, D. Hardacre, H. Li, Mater. Sci. Eng. A **703**, 251–261 (2017). https://doi.org/10.1016/j.msea.2017.07.071
91. H. Zhang, C. Li, M. Xu, W. Dai, P. Kumar, Z. Liu, Z. Li, Y. Zhang, Mater. Sci. Eng. A **802**, 140640 (2021). https://doi.org/10.1016/j.msea.2020.140640
92. J.W. Pegues, M.D. Roach, N. Shamsaei, Mater. Res. Lett. **8**, 8–15 (2020). https://doi.org/10.1080/21663831.2019.1678202
93. J.R. Trelewicz, G.P. Halada, O.K. Donaldson, G. Manogharan, JOM **68**, 850–859 (2016). https://doi.org/10.1007/s11837-016-1822-4
94. Q. Chao, V. Cruz, S. Thomas, N. Birbilis, P. Collins, A. Taylor, P.D. Hodgson, D. Fabijanic, Scripta Mater. **141**, 94–98 (2017). https://doi.org/10.1016/j.scriptamat.2017.07.037
95. J. Stewart, D.E. Williams, Corros. Sci. **33**, 457–474 (1992). https://doi.org/10.1016/0010-938X(92)90074-D
96. G. Sander, S. Thomas, V. Cruz, M. Jurg, N. Birbilis, X. Gao, M. Brameld, C.R. Hutchinson, J. Electrochem. Soc. **164**, C250–C257 (2017). https://doi.org/10.1149/2.0551706jes
97. M. Kazemipour, M. Mohammadi, E. Mfoumou, A. Nasiri, JOM **71**, 3230–3240 (2019). https://doi.org/10.1007/s11837-019-03647-w
98. Y. Sun, A. Moroz, K. Alrbaey, J. Mater. Eng. Perform. **23**, 518–526 (2014). https://doi.org/10.1007/s11665-013-0784-8
99. D. Kong, X. Ni, C. Dong, X. Lei, L. Zhang, C. Man, J. Yao, X. Cheng, X. Li, Mater. Des. **152**, 88–101 (2018). https://doi.org/10.1016/j.matdes.2018.04.058
100. M. Laleh, A.E. Hughes, W. Xu, N. Haghdadi, K. Wang, P. Cizek, I. Gibson, M.Y. Tan, Corros. Sci. **161**, 108189 (2019). https://doi.org/10.1016/j.corsci.2019.108189
101. W.M. Garrison, M.O.H. Amuda, *Reference Module in Materials Science and Materials Engineering* (Elsevier, 2017)
102. A.F. Candelaria, C.E. Pinedo, J. Mater. Sci. Lett. **22**, 1151–1153 (2003). https://doi.org/10.1023/A:1025179128333
103. L. Zai, C. Zhang, Y. Wang, W. Guo, D. Wellmann, X. Tong, Y. Tian, Metals **10**, 255 (2020). https://doi.org/10.3390/met10020255
104. I. Kartikeya Sarma, N. Selvraj, A. Kumar, *Recent Advances in Manufacturing Processes and Systems* (Springer, Berlin, 2022), pp.37–53
105. B. Lv, F. Wang, X. Niu, L. Zhang, X. Wu, Y. Lai, B. Hong, S. Cao, Mater. Sci. Eng. A **847**, 143340 (2022). https://doi.org/10.1016/j.msea.2022.143340
106. X. Zhao, Q. Wei, B. Song, Y. Liu, X. Luo, S. Wen, Y. Shi, Mater. Manuf. Process. **30**, 1283–1289 (2015). https://doi.org/10.1080/10426914.2015.1026351
107. S.D. Nath, H. Irrinki, G. Gupta, M. Kearns, O. Gulsoy, S. Atre, Powder Technol. **343**, 738–746 (2019). https://doi.org/10.1016/j.powtec.2018.11.075
108. X. Yan, C. Chen, C. Chang, D. Dong, R. Zhao, R. Jenkins, J. Wang, Z. Ren, M. Liu, H. Liao, R. Lupoi, S. Yin, Mater. Sci. Eng. A **781**, 139227 (2020). https://doi.org/10.1016/j.msea.2020.139227
109. S. Cheruvathur, E.A. Lass, C.E. Campbell, JOM **68**, 930–942 (2016). https://doi.org/10.1007/s11837-015-1754-4
110. B. AlMangour, J.-M. Yang, Int. J. Adv. Manuf. Technol. **90**, 119–126 (2017). https://doi.org/10.1007/s00170-016-9367-9

111. H.K. Rafi, D. Pal, N. Patil, T.L. Starr, B.E. Stucker, J. Mater. Eng. Perform. **23**, 4421–4428 (2014). https://doi.org/10.1007/s11665-014-1226-y
112. Y. Sun, R.J. Hebert, M. Aindow, Mater. Des. **156**, 429–440 (2018). https://doi.org/10.1016/j.matdes.2018.07.015
113. J.-R. Lee, M.-S. Lee, H. Chae, S.Y. Lee, T. Na, W.-S. Kim, T.-S. Jun, Mater. Charact. **167**, 110468 (2020). https://doi.org/10.1016/j.matchar.2020.110468
114. K. Li, J. Zhan, T. Yang, A.C. To, S. Tan, Q. Tang, H. Cao, L.E. Murr, Addit. Manuf. **52**, 102672 (2022). https://doi.org/10.1016/j.addma.2022.102672
115. T.-H. Hsu, Y.-J. Chang, C.-Y. Huang, H.-W. Yen, C.-P. Chen, K.-K. Jen, A.-C. Yeh, J. Alloys Compd. **803**, 30–41 (2019). https://doi.org/10.1016/j.jallcom.2019.06.289
116. S. Vunnam, A. Saboo, C. Sudbrack, T.L. Starr, Addit. Manuf. **30**, 100876 (2019). https://doi.org/10.1016/j.addma.2019.100876
117. M. Alnajjar, F. Christien, K. Wolski, C. Bosch, Addit. Manuf. **25**, 187–195 (2019). https://doi.org/10.1016/j.addma.2018.11.004
118. L.F. Kultz Unti, L.S. Aota, A.L. Jardini, A.P. Tschiptschin, H.R.Z. Sandim, E.A. Jägle, K.D. Zilnyk, Mater. Charact. **181**, 111485 (2021). https://doi.org/10.1016/j.matchar.2021.111485
119. L. Facchini, N. Vicente, I. Lonardelli, E. Magalini, P. Robotti, A. Molinari, Adv. Eng. Mater. **12**, 184–188 (2010). https://doi.org/10.1002/adem.200900259
120. A. Yadollahi, N. Shamsaei, S.M. Thompson, A. Elwany, L. Bian, Int. J. Fatigue **94**, 218–235 (2017). https://doi.org/10.1016/j.ijfatigue.2016.03.014
121. X.D. Nong, X.L. Zhou, Mater. Charact. **174**, 111012 (2021). https://doi.org/10.1016/j.matchar.2021.111012
122. S. Sabooni, A. Chabok, S.C. Feng, H. Blaauw, T.C. Pijper, H.J. Yang, Y.T. Pei, Addit. Manuf. **46**, 102176 (2021). https://doi.org/10.1016/j.addma.2021.102176
123. S. Pasebani, M. Ghayoor, S. Badwe, H. Irrinki, S.V. Atre, Addit. Manuf. **22**, 127–137 (2018). https://doi.org/10.1016/j.addma.2018.05.011
124. L.E. Murr, E. Martinez, J. Hernandez, S. Collins, K.N. Amato, S.M. Gaytan, P.W. Shindo, J. Mater. Res. Technol. **1**, 167–177 (2012). https://doi.org/10.1016/S2238-7854(12)70029-7
125. R. Rashid, S.H. Masood, D. Ruan, S. Palanisamy, R.A. Rahman Rashid, M. Brandt, J. Mater. Process. Technol. **249**, 502–511 (2017). https://doi.org/10.1016/j.jmatprotec.2017.06.023
126. H.R. Habibi Bajguirani, Mater. Sci. Eng. A **338**, 142–159 (2002). https://doi.org/10.1016/S0921-5093(02)00062-X
127. X.D. Nong, X.L. Zhou, J.H. Li, Y.D. Wang, Y.F. Zhao, M. Brochu, Scripta Mater. **178**, 7–12 (2020). https://doi.org/10.1016/j.scriptamat.2019.10.040
128. T. LeBrun, T. Nakamoto, K. Horikawa, H. Kobayashi, Mater. Des. **81**, 44–53 (2015). https://doi.org/10.1016/j.matdes.2015.05.026
129. S. Sarkar, S. Mukherjee, C.S. Kumar, A. Kumar Nath, J. Manuf. Process. **50**, 279–294 (2020). https://doi.org/10.1016/j.jmapro.2019.12.048
130. S. Sarkar, C.S. Kumar, A.K. Nath, J. Manuf. Sci. Eng. **139**, 111010 (2017). https://doi.org/10.1115/1.4037437
131. Q. Shi, F. Qin, K. Li, X. Liu, G. Zhou, Mater. Sci. Eng. A **810**, 141035 (2021). https://doi.org/10.1016/j.msea.2021.141035
132. S. Sarkar, C.S. Kumar, A.K. Nath, Mater. Sci. Eng. A **755**, 235–245 (2019). https://doi.org/10.1016/j.msea.2019.04.003
133. P.D. Nezhadfar, K. Anderson-Wedge, S.R. Daniewicz, N. Phan, S. Shao, N. Shamsaei, Addit. Manuf. **36**, 101604 (2020). https://doi.org/10.1016/j.addma.2020.101604
134. M.R. Stoudt, R.E. Ricker, E.A. Lass, L.E. Levine, JOM **69**, 506–515 (2017). https://doi.org/10.1007/s11837-016-2237-y
135. C. Garcia-Cabezon, M.A. Castro-Sastre, A.I. Fernandez-Abia, M.L. Rodriguez-Mendez, F. Martin-Pedrosa, Met. Mater. Int. **28**, 2652–2667 (2022). https://doi.org/10.1007/s12540-021-01155-8
136. H. Irrinki, T. Harper, S. Badwe, J. Stitzel, O. Gulsoy, G. Gupta, S.V. Atre, Prog. Addit. Manuf. **3**, 39–49 (2018). https://doi.org/10.1007/s40964-018-0048-0
137. L. Wang, C. Dong, C. Man, D. Kong, K. Xiao, X. Li, Corros. Sci. **166**, 108427 (2020). https://doi.org/10.1016/j.corsci.2019.108427
138. P. Krakhmalev, I. Yadroitsava, G. Fredriksson, I. Yadroitsev, Mater. Des. **87**, 380–385 (2015). https://doi.org/10.1016/j.matdes.2015.08.045
139. K. Saeidi, D.L. Zapata, F. Lofaj, L. Kvetkova, J. Olsen, Z. Shen, F. Akhtar, Addit. Manuf. **29**, 100803 (2019). https://doi.org/10.1016/j.addma.2019.100803
140. E. Liverani, A. Fortunato, Int. J. Adv. Manuf. Technol. **117**, 809–821 (2021). https://doi.org/10.1007/s00170-021-07639-6
141. M. Liljas, P. Johansson, H.P. Liu, C.O.A. Olsson, Steel Res. Int. **79**, 466–473 (2008). https://doi.org/10.1002/srin.200806154
142. K. Saeidi, L. Kevetkova, F. Lofaj, Z. Shen, Mater. Sci. Eng. A **665**, 59–65 (2016). https://doi.org/10.1002/srin.200806154
143. H. Tan, Y. Jiang, B. Deng, T. Sun, J. Xu, J. Li, Mater. Charact. **60**, 1049–1054 (2009). https://doi.org/10.1016/j.matchar.2009.04.009
144. M. Knyazeva, M. Pohl, Metallography. Microstruct. Anal. **2**, 343–351 (2013). https://doi.org/10.1007/s13632-013-0088-2
145. F. Hengsbach, P. Koppa, K. Duschik, M.J. Holzweissig, M. Burns, J. Nellesen, W. Tillmann, T. Tröster, K.-P. Hoyer, M. Schaper, Mater. Des. **133**, 136–142 (2017). https://doi.org/10.1016/j.matdes.2017.07.046
146. O. Andreau, I. Koutiri, P. Peyre, J.-D. Penot, N. Saintier, E. Pessard, T. De Terris, C. Dupuy, T. Baudin, J. Mater. Process. Technol. **264**, 21–31 (2019). https://doi.org/10.1016/j.jmatprotec.2018.08.049
147. S. Papula, M. Song, A. Pateras, X.-B. Chen, M. Brandt, M. Easton, Y. Yagodzinskyy, I. Virkkunen, H. Hänninen, Materials **12**, 2468 (2019). https://doi.org/10.3390/ma12152468
148. E.B. Fonseca, A.H. Gabriel, L.C. Araújo, P.L. Santos, K.N. Campo, E.S. Lopes, Addit. Manuf. **34**, 101250 (2020). https://doi.org/10.1016/j.addma.2020.101250
149. M. Mirz, S. Herzog, C. Broeckmann, A. Kaletsch, J. Manuf. Mater. Process. **6**, 32 (2022). https://doi.org/10.3390/jmmp6020032
150. K.M. Bertsch, G.M. de Bellefon, B. Kuehl, D.J. Thoma, Acta Mater. **199**, 19–33 (2020). https://doi.org/10.1016/j.actamat.2020.07.063
151. H. Miura, M. Kobayashi, C. Watanabe, N. Sugiura, N. Yoshinaga, Mater. Trans. **61**, 416–419 (2020). https://doi.org/10.2320/matertrans.MT-M2019302
152. R. Mondal, S.K. Bonagani, P. Raut, S. Kumar, P.V. Sivaprasad, G. Chai, V. Kain, I. Samajdar, J. Mater. Eng. Perform. **31**, 1478–1492 (2022). https://doi.org/10.1007/s11665-021-06221-1
153. Y. Yang, H. Tan, Z. Zhang, Z. Wang, Y. Jiang, L. Jiang, J. Li, Corrosion **69**, 167–173 (2013). https://doi.org/10.5006/0717
154. G.N. Nigon, O.B. Isgor, S. Pasebani, J. Electrochem. Soc. **167**, 141508 (2020). https://doi.org/10.1149/1945-7111/abc5dd
155. S. Jeffs, R. Douglas, W. Beard, M. Coleman, J. Adams, T. Jones, D. Poole, R. Lancaster, Mater. Charact. **189**, 111953 (2022)
156. K. Davidson, S. Singamneni, Mater. Manuf. Process. **31**, 1543–1555 (2016). https://doi.org/10.1080/10426914.2015.1090605
157. F. Shang, X. Chen, Z. Wang, Z. Ji, F. Ming, S. Ren, X. Qu, Metals **9**, 1012 (2019). https://doi.org/10.3390/met9091012
158. J. Zhang, H. Dong, X. Xi, H. Tang, X. Li, J.H. Rao, Z. Xiao, Scripta Mater. **237**, 115711 (2023). https://doi.org/10.1016/j.scriptamat.2023.115711
159. P.F. Jiang, C.H. Zhang, S. Zhang, J.B. Zhang, J. Chen, H.T. Chen, Opt. Laser Technol. **140**, 107055 (2021). https://doi.org/10.1016/j.optlastec.2021.107055

160. E. Vasquez, P.-F. Giroux, F. Lomello, A. Chniouel, H. Maskrot, F. Schuster, P. Castany, J. Mater. Process. Technol. **267**, 403–413 (2019). https://doi.org/10.1016/j.jmatprotec.2018.12.034
161. A. Wasilkowska, M. Bartsch, U. Messerschmidt, R. Herzog, A. Czyrska-Filemonowicz, J. Mater. Process. Technol. **133**, 218–224 (2003). https://doi.org/10.1016/S0924-0136(02)00237-6
162. D. Karlsson, C.-Y. Chou, N.H. Pettersson, T. Helander, P. Harlin, M. Sahlberg, G. Lindwall, J. Odqvist, U. Jansson, Addit. Manuf. **36**, 101580 (2020). https://doi.org/10.1016/j.addma.2020.101580
163. J.C. Walker, K.M. Berggreen, A.R. Jones, C.J. Sutcliffe, Adv. Eng. Mater. **11**, 541–546 (2009). https://doi.org/10.1002/adem.200800407
164. T. Boegelein, S.N. Dryepondt, A. Pandey, K. Dawson, G.J. Tatlock, Acta Mater. **87**, 201–215 (2015). https://doi.org/10.1016/j.actamat.2014.12.047
165. K. Munir, A. Biesiekierski, C. Wen, Y. Li, in *Metallic Biomaterials Processing and Medical Device Manufacturing*. ed. by C. Wen (Woodhead Publishing, Cambridge, 2020), pp. 235–269
166. N.T. Aboulkhair, N.M. Everitt, I. Ashcroft, C. Tuck, Addit. Manuf. **1-4**, 77–86 (2014). https://doi.org/10.1016/j.addma.2014.08.001
167. SANDVIK, Stainless Steels (2022), https://www.metalpowder.sandvik/en/products/metal-powder-alloys/stainless-steels/. Accessed 17 Mar 2022
168. Q.B. Nguyen, Z. Zhu, F.L. Ng, B.W. Chua, S.M.L. Nai, J. Wei, Mater. Sci. Technol. **35**, 388–394 (2019). https://doi.org/10.1016/j.jmst.2018.10.013
169. H.H. Alsalla, C. Smith, L. Hao, Rapid Prototyp. J. **24**, 9–17 (2018). https://doi.org/10.1108/RPJ-04-2016-0068
170. L. Hitzler, J. Hirsch, B. Heine, M. Merkel, W. Hall, A. Öchsner, Materials **10**, 1136 (2017). https://doi.org/10.3390/ma10101136
171. ASTM A276-10, Standard Specification for Stainless Steel Bars and Shapes (ASTM International, West Conshohocken, 2011), https://doi.org/10.1520/A0276-10
172. Z. Hu, H. Zhu, H. Zhang, X. Zeng, Opt. Laser Technol. **87**, 17–25 (2017). https://doi.org/10.1016/j.optlastec.2016.07.012
173. H.K. Rafi, T.L. Starr, B.E. Stucker, Int. J. Adv. Manuf. Technol. **69**, 1299–1309 (2013). https://doi.org/10.1007/s00170-013-5106-7
174. ASTM A693-16, Standard Specification for Precipitation-Hardening Stainless and Heat-Resisting Steel Plate, Sheet, and Strip (ASTM International, West Conshohocken, 2019), https://doi.org/10.1520/A0693-16R22